



HAL
open science

On the coupling of a direct-forcing immersed boundary method and the regularized lattice Boltzmann method for fluid-structure interaction

Zhe Li, Wenjin Cao, David Le Touzé

► **To cite this version:**

Zhe Li, Wenjin Cao, David Le Touzé. On the coupling of a direct-forcing immersed boundary method and the regularized lattice Boltzmann method for fluid-structure interaction. *Computers and Fluids*, 2019, 190, pp.470-484. 10.1016/j.compfluid.2019.06.030 . hal-02280690

HAL Id: hal-02280690

<https://hal.science/hal-02280690>

Submitted on 25 Oct 2021

HAL is a multi-disciplinary open access archive for the deposit and dissemination of scientific research documents, whether they are published or not. The documents may come from teaching and research institutions in France or abroad, or from public or private research centers.

L'archive ouverte pluridisciplinaire **HAL**, est destinée au dépôt et à la diffusion de documents scientifiques de niveau recherche, publiés ou non, émanant des établissements d'enseignement et de recherche français ou étrangers, des laboratoires publics ou privés.



Distributed under a Creative Commons Attribution - NonCommercial 4.0 International License

On the coupling of a direct-forcing immersed boundary method and the regularized lattice Boltzmann method for fluid-structure interaction

Zhe Li*, Wenjin Cao, David Le Touzé

^a*Ecole Centrale Nantes, LHEEA Research dept. (ECN and CNRS), Nantes, France*

Abstract

The present paper provides an analysis of the force model effect on the regularization procedure based on the Hermite expansion in regularized lattice Boltzmann method (RLBM). It is shown that, when using the 2nd-order accurate in time semi-implicit force model of Guo et al. [15] in RLBM, the reconstruction of the non-equilibrium part of the distribution function has to start from the 1st-order Hermite polynomial, because the new distribution function (after a change of variables) contains the body force effect. Based on this Hermite regularization, an immersed boundary-regularized lattice Boltzmann (IB-RLB) coupling method is proposed for simulating transient fluid-structure interactions (FSI) with rigid and deformable solid objects. The fluid and solid solvers are coupled in a non-staggered way so that the stability and accuracy are well preserved. The proposed IB-RLB coupling method is then validated with several numerical test-cases, such as impulsively started plate, vortex-induced vibrations and 3D flapping flag, for which good agreements are found with the references.

Keywords: Fluid-structure interaction, Immersed boundary method, Regularized lattice Boltzmann method, Force model

1. Introduction

Fluid-structure interaction (FSI) problems are widely present in nature and engineering applications, such as blood flows through the heart valves, wind-tall building interaction, etc. Hence it is of great interest and importance to have an accurate and robust numerical tool for better understanding the underlying physics and providing methods to industrial engineerings. Over the two decades, the lattice Boltzmann method (LBM) emerged as a promising numerical method possessing attractive features, such as its kinetic origin making it capable of simulating problems within a large range of Knudsen number (i.e. beyond just those obeying the Navier-Stokes equations), high computational efficiency (highly parallelizable), etc.

*Corresponding author
Email address: zhe.li@ec-nantes.fr (Zhe Li)

The standard LB (SLB) scheme [20, 40] is based on the single-relaxation-time (SRT) Bhatnagar-Gross-Krook (BGK) [3] collision model. Although this SRT-BGK SLB scheme is widely used because of its simplicity and efficiency, it was found to develop sometimes numerical instabilities, which might be induced by non-adapted initial condition, geometric singularities or inaccurate numerical approximations [41], even at very moderate Reynolds numbers. In this context, several stabilization techniques have been proposed in the literature, such as the multi-relaxation-time (MRT) collision model [26], entropic LB method (ELBM) [1] and entropic stabilizer [22], and the regularized LBM (RLBM) [27, 54]. In this paper, we will apply the regularization procedure as stabilization technique for the numerical simulation of FSI problems.

The regularization procedure in LBM consists in filtering out the effect of the undesired ghost modes which might generate numerical instabilities [45]. Different regularization techniques have been proposed and investigated in the literature [5, 25, 27, 34, 36, 54]. For example, through the Chapman-Enskog analysis [4], Latt and Chopard [27] proposed to reconstruct the non-equilibrium part of the pre-collision distribution function using the gradient of the macroscopic fluid velocity. It is found that this regularization procedure can considerably increase the maximal Reynolds number which can be simulated in a stable way for a given lattice size [27]. Based on this idea, Latt et al. [28] proposed a straight velocity boundary condition treatment. Besides, it is also possible to reconstruct the non-equilibrium part by means of the Hermite polynomial expansion [14]. In 2006, Shan et al. [43] demonstrated that the lattice Boltzmann equation (LBE) can be systematically derived from the Boltzmann equation, with the help of the Hermite polynomials. In the same year, Zhang et al. [54] proposed a regularization procedure based on the projection of the non-equilibrium part of the pre-collision distribution function onto the Hilbert sub-space spanned by the Hermite polynomials. In fact, the regularization formula of Latt and Chopard [27] can also be derived using Hermite polynomial expansion, as shown in Appendix. Here we adopt the regularization procedure based on the Hermite polynomial expansion for stabilizing the FSI simulation, because of (i) its systematic link with the kinetic theory; (ii) the *a priori* and consistent derivations of the distribution function (equilibrium and non-equilibrium parts) and of the body force term; and (iii) its potential for straightforward extension to high-order LBM [6, 35], although only weakly-compressible isothermal fluid flows are considered in the present paper.

As mentioned previously, the body force term in the LBE can also be obtained by means of the Hermite polynomial expansion of the external acceleration in the continuous Boltzmann equation [33]. This force model has been initially derived by Martys et al. [33] and then adopted by Zhang et al. [54] in their Hermite regularization procedure. However, it can be shown that the time integration of the force term in [54] is treated with an explicit 1st-order scheme. Indeed, as investigated by Guo et al. [15], this force model [33] does generate some extra errors under the Chapman-Enskog analysis, compared with the one proposed by Guo et al. [15] which is obtained in an *a postepriori* way [43] aiming at canceling the leading errors. In 2007, by using the

Hermite polynomial expansion and a change of variables [18], Guo et al. [16] demonstrated that the force model [15] can be derived in a systematic and *a priori* way. In [16] one can easily observe that the time integration of the force term is treated with the 2nd-order accurate trapezoidal scheme. In the present paper, we adopt this 2nd-order force model [15, 16] and will discuss the force model effect on the regularization procedure in RLBM.

Indeed, accurately incorporating body force effects in LBM is important for simulating fluid flows in the presence of external body force, such as the gravity, or for coupling with a direct-forcing immersed boundary method (IBM) for FSI problems. In [54], it is suggested to start the regularization directly from the 2nd-order Hermite polynomial, since the 0th- and 1st-order Hermite expansion coefficients are both equal to zero by construction. However, this is true only with the 1st-order accurate in time explicit force model [33, 54]. When using the 2nd-order semi-implicit force model of Guo et al. [15, 16], a change of variables is performed in order to get the fully discrete LBE [18] in an equivalent but explicit form. We observe that the newly defined distribution function that is streamed in the LB solver contains the effect of body force. As a result, the regularization has to be started from the 1st-order Hermite polynomial instead of the 2nd-order one.

In the present paper, with the help of a systematic derivation of the force model of Guo et al. [15] using the Hermite polynomial expansion, we demonstrate the effect of the choice of the force model on the regularization procedure and the necessity of starting the reconstruction of the non-equilibrium part of the pre-collision distribution from the 1st-order Hermite expansion. To the best of our knowledge, this point has not been reported in the literature of the Hermite RLBM mentioned above. Based on this regularization technique, we propose to couple the RLBM with a direct-forcing IBM, in a non-staggered way, for the numerical simulation of FSI problems in the presence of moving rigid/deformable solid structures. Through some numerical validations we observe that this regularization procedure allows us to significantly enhance the numerical stability and eliminate undesired spurious noises (see Figure 4) in these FSI problems.

The rest of the paper is organized as follows: Section 2 shows the effect of the force model on the regularization procedure in RLBM. Some necessary details of the adopted IBM are then provided in Section 3. A non-staggered IB-RLB coupling algorithm for FSI problems is proposed in Section 4. Several numerical validations are presented in Section 5. Finally, the conclusions are drawn in Section 6.

2. Regularized lattice Boltzmann method

2.1. Lattice Boltzmann equation with force term

2.1.1. Discrete Boltzmann equation

The discrete Boltzmann equation based on the BGK collision model is written as [43]

$$\frac{\partial f_a}{\partial t} + \boldsymbol{\xi}_a \cdot \frac{\partial f_a}{\partial \boldsymbol{x}} = -\frac{1}{\tau} (f_a - f_a^{eq}) + F_a, \quad (1)$$

where $f_a = f_a(\mathbf{x}, t)$ denotes the distribution function at the position \mathbf{x} and time t , corresponding to the a^{th} discrete lattice velocity $\boldsymbol{\xi}_a$, τ the relaxation time, $f_a^{eq} = f_a^{eq}(\mathbf{x}, t)$ the equilibrium distribution function and $F_a = F_a(\mathbf{x}, t)$ the external force term.

The equilibrium distribution function f_a^{eq} can be obtained from the Hermite expansion of the Maxwell-Boltzmann distribution function

$$f_a^{eq} = \rho w_a \left(1 + \frac{\boldsymbol{\xi}_a \cdot \mathbf{v}}{c_s^2} + \frac{(\boldsymbol{\xi}_a \cdot \mathbf{v})^2}{2c_s^4} - \frac{\mathbf{v} \cdot \mathbf{v}}{2c_s^2} \right), \quad (2)$$

where w_a is the weight coefficient, c_s is the speed of sound. In addition, $\rho = \rho(\mathbf{x}, t)$ and $\mathbf{v} = \mathbf{v}(\mathbf{x}, t)$ denote respectively the macroscopic fluid density and velocity, with the following definitions

$$\begin{cases} \rho = \sum_a f_a = \sum_a f_a^{eq}, \\ \rho \mathbf{v} = \sum_a f_a \boldsymbol{\xi}_a = \sum_a f_a^{eq} \boldsymbol{\xi}_a. \end{cases} \quad (3)$$

Moreover, the force term F_a in Equation (1) can also be derived by means of the Hermite expansion [33]

$$F_a = w_a \left(\frac{\boldsymbol{\xi}_a - \mathbf{v}}{c_s^2} + \frac{(\boldsymbol{\xi}_a \cdot \mathbf{v})}{c_s^4} \boldsymbol{\xi}_a \right) \cdot \mathbf{F}, \quad (4)$$

where $\mathbf{F} = \mathbf{F}(\mathbf{x}, t) = \rho(\mathbf{x}, t) \mathbf{g}(\mathbf{x}, t)$ is the external body force (per unit volume) exerted inside the fluid domain, with $\mathbf{g}(\mathbf{x}, t)$ being the acceleration in the Boltzmann equation. The first two moments of F_a are given as

$$\begin{cases} \sum_a F_a = 0, \\ \sum_a F_a \boldsymbol{\xi}_a = \mathbf{F}. \end{cases} \quad (5)$$

It is worth noting here that the equilibrium distribution function f_a^{eq} in Equation (2) and the force term F_a in Equation (4) are both expanded with Hermite polynomials and truncated up to 2nd-order, which is sufficient for describing weakly-compressible isothermal fluid flows [16].

2.1.2. Force model in lattice Boltzmann equation

In order to derive the lattice Boltzmann equation with 2nd-order accuracy, He et al. [18] proposed to integrate the discrete Boltzmann equation (1) along the characteristic line (or the lattice velocity) over one time-step Δt as

$$f_a(\mathbf{x} + \boldsymbol{\xi}_a \Delta t, t + \Delta t) - f_a(\mathbf{x}, t) = \frac{\Delta t}{2} \left(-\frac{1}{\tau} (f_a(\mathbf{x}, t) - f_a^{eq}(\mathbf{x}, t)) + F_a(\mathbf{x}, t) \right) + \frac{\Delta t}{2} \left(-\frac{1}{\tau} (f_a(\mathbf{x} + \boldsymbol{\xi}_a \Delta t, t + \Delta t) - f_a^{eq}(\mathbf{x} + \boldsymbol{\xi}_a \Delta t, t + \Delta t)) + F_a(\mathbf{x} + \boldsymbol{\xi}_a \Delta t, t + \Delta t) \right), \quad (6)$$

where the right hand side of Equation (1) is integrated over one time-step using the trapezoidal rule which ensures the 2nd-order accuracy of this implicit lattice Boltzmann equation (6).

By means of a change of variables [9, 18], an equivalent but explicit version of Equation (6) can be obtained as

$$\bar{f}_a(\mathbf{x} + \boldsymbol{\xi}_a \Delta t, t + \Delta t) - \bar{f}_a(\mathbf{x}, t) = -\frac{\Delta t}{\bar{\tau}} (\bar{f}_a(\mathbf{x}, t) - f_a^{eq}(\mathbf{x}, t)) + \Delta t \left(1 - \frac{\Delta t}{2\bar{\tau}}\right) F_a(\mathbf{x}, t), \quad (7)$$

where $\bar{\tau} = \tau + 0.5\Delta t$ is the new relaxation time and the new distribution function $\bar{f}_a(\mathbf{x}, t)$ is defined as

$$\bar{f}_a(\mathbf{x}, t) = \left(1 + \frac{\Delta t}{2\tau}\right) f_a(\mathbf{x}, t) - \frac{\Delta t}{2\tau} f_a^{eq}(\mathbf{x}, t) - \frac{\Delta t}{2} F_a(\mathbf{x}, t), \quad (8)$$

of which the first two moments are given as

$$\begin{cases} \sum_a \bar{f}_a = \sum_a f_a - \frac{\Delta t}{2} \sum_a F_a = \rho, \\ \sum_a \bar{f}_a \boldsymbol{\xi}_a = \sum_a f_a \boldsymbol{\xi}_a - \frac{\Delta t}{2} \sum_a F_a \boldsymbol{\xi}_a = \rho \mathbf{v} - \frac{\Delta t}{2} \mathbf{F}. \end{cases} \quad (9)$$

As indicated in [16], this lattice Boltzmann equation (7) with force term is just the same as the one proposed in [15], in which the coefficients are determined via *a posteriori* matching [43] in order to eliminate the errors related to the body force term.

Now, let us rewrite Equations (7)-(9) in a more general form for the force term by introducing a coefficient θ , as follows

$$\bar{f}_a(\mathbf{x} + \boldsymbol{\xi}_a \Delta t, t + \Delta t) - \bar{f}_a(\mathbf{x}, t) = -\frac{\Delta t}{\bar{\tau}} (\bar{f}_a(\mathbf{x}, t) - f_a^{eq}(\mathbf{x}, t)) + \Delta t \left(1 - \theta \frac{\Delta t}{\bar{\tau}}\right) F_a(\mathbf{x}, t), \quad (10)$$

where the new distribution function is defined as

$$\bar{f}_a(\mathbf{x}, t) = \left(1 + \frac{\Delta t}{2\tau}\right) f_a(\mathbf{x}, t) - \frac{\Delta t}{2\tau} f_a^{eq}(\mathbf{x}, t) - \theta \Delta t F_a(\mathbf{x}, t), \quad (11)$$

of which the first two moments are calculated as

$$\begin{cases} \sum_a \bar{f}_a = \sum_a f_a - \frac{\Delta t}{2} \sum_a F_a = \rho, \\ \sum_a \bar{f}_a \boldsymbol{\xi}_a = \sum_a f_a \boldsymbol{\xi}_a - \theta \Delta t \sum_a F_a \boldsymbol{\xi}_a = \rho \mathbf{v} - \theta \Delta t \mathbf{F}. \end{cases} \quad (12)$$

In Equations (10)-(12) one may observe that adopting different values of θ leads to different integration schemes for the force term:

- (a) *Explicit scheme* ($\theta = 0$): It is the force model firstly proposed by Martys et al. [33], which is adopted by Zhang et al. [54] in their Hermite regularization procedure. We observe that the time integration of the force term $F_a(\mathbf{x}, t)$ over one time-step is treated with a 1st-order explicit scheme. Since $\theta = 0$, the first two moments of \bar{f}_a , Equation (12), are the same as the ones of f_a , hence there is no need to take into account the body force effect when calculating the macroscopic velocity. However, by means of the Chapman-Enskog analysis, Guo et al. [15] showed that this explicit scheme introduces some errors in the presence of a time-varying non-uniform body force.

- (b) *Semi-implicit scheme* ($\theta = 0.5$): It is the force model previously shown in Equations (7)-(8), which is proposed by Guo et al. [15, 16]. As shown in Equation (6), the collision and force terms are both integrated in time using a 2nd-order trapezoidal scheme [18]. Guo et al. [15] showed that this force model introduces the lowest errors among the existing force models in the literature.
- (c) *Implicit scheme* ($\theta = 1$): The last case uses a fully implicit scheme for integrating the force term in time along the characteristic line, which is however 1st-order accurate in time and also needs to consider the body force effect in the computation of macroscopic velocity.

In the present work, we choose to adopt the semi-implicit force model (b) with $\theta = 0.5$, proposed by Guo et al. [15, 16], because: (i) it can be systematically derived from the discrete Boltzmann equation (1) with the help of Hermite expansions; (ii) 2nd-order accuracy can be assured via a change of variables; (iii) based on the Chapman-Enskog analysis on different force models in [15], it introduces less errors than the others, especially when the body force is not constant in space and time; (iv) it splits the macroscopic velocity into two parts as $\rho\mathbf{v} = \sum_a \bar{f}_a \boldsymbol{\xi}_a + 0.5\Delta t \mathbf{F}$, which is an advantage for coupling with a direct-forcing immersed boundary method.

2.2. Regularization procedure

2.2.1. Expansion based on the Hermite polynomials

The distribution function $f_a(\mathbf{x}, t)$ (discrete in velocity space but continuous in configuration space and time) can be expanded into a truncated series (up to N^{th} -order) based on the Hermite polynomials [14, 43]

$$f_a(\mathbf{x}, t) \simeq \hat{f}_a(\mathbf{x}, t) = w_a \sum_{n=0}^N \frac{1}{n!} \hat{\mathbf{a}}^{(n)}(\mathbf{x}, t) : \mathcal{H}^{(n)}(\boldsymbol{\xi}_a), \quad (13)$$

where ‘:’ denotes full contraction and the n^{th} -order expansion coefficient $\hat{\mathbf{a}}^{(n)}(\mathbf{x}, t)$ is computed as

$$\hat{\mathbf{a}}^{(n)}(\mathbf{x}, t) = \mathbf{a}^{(n)}(\mathbf{x}, t) = \sum_a f_a(\mathbf{x}, t) \mathcal{H}^{(n)}(\boldsymbol{\xi}_a). \quad (14)$$

It is here worth noting that $f_a(\mathbf{x}, t)$ and $\hat{f}_a(\mathbf{x}, t)$ have the same first N expansion coefficients, i.e. $\hat{\mathbf{a}}^{(n)}(\mathbf{x}, t) \equiv \mathbf{a}^{(n)}(\mathbf{x}, t)$, where $\forall n \leq N$, because of the orthogonality of Hermite polynomials.

In addition, the first few Hermite polynomials are given as

$$\begin{cases} \mathcal{H}_a^{(0)} = \mathcal{H}^{(0)}(\boldsymbol{\xi}_a) = 1, \\ \mathcal{H}_a^{(1)} = \mathcal{H}^{(1)}(\boldsymbol{\xi}_a) = \frac{\boldsymbol{\xi}_a}{c_s}, \\ \mathcal{H}_a^{(2)} = \mathcal{H}^{(2)}(\boldsymbol{\xi}_a) = \frac{\boldsymbol{\xi}_a \otimes \boldsymbol{\xi}_a}{c_s^2} - \mathbf{I}. \end{cases} \quad (15)$$

2.2.2. Hermite regularization of the non-equilibrium part of the distribution function

In the adopted force scheme presented in Section 2.1, the collision and streaming operations are carried out with the distribution function \bar{f}_a . After each streaming step, at the instant t , a local position \mathbf{x} possesses the distribution function $\bar{f}_a(\mathbf{x}, t)$ streamed from the neighboring lattice nodes. Generally, this \bar{f}_a does not entirely lie in the sub-space spanned by the first N leading Hermite basis [54], i.e. \bar{f}_a may contain higher-order components that are not useful for recovering Navier-Stokes equation but might destabilize the numerical simulation of LBM.

Splitting the distribution function \bar{f}_a into an equilibrium part f_a^{eq} and a non-equilibrium part \bar{f}_a^{neq} , we can extract the non-equilibrium part as

$$\bar{f}_a^{neq} = \bar{f}_a - f_a^{eq}, \quad (16)$$

where \bar{f}_a^{neq} is the part that contains undesired higher-order components, since f_a^{eq} is expanded with the Hermite polynomials up to N^{th} -order.

Following the idea proposed in [54], after each streaming step, we replace \bar{f}_a^{neq} by \hat{f}_a^{neq} which is a Hermite expansion series truncated at N^{th} -order

$$\hat{f}_a^{neq} = w_a \sum_{n=0}^N \frac{1}{n!} \hat{\mathbf{a}}_{neq}^{(n)} : \mathcal{H}_a^{(n)}, \quad (17)$$

with the n^{th} -order ($n \leq N$) expansion coefficient computed as

$$\hat{\mathbf{a}}_{neq}^{(n)} = \mathbf{a}_{neq}^{(n)} = \sum_a \bar{f}_a^{neq} \mathcal{H}_a^{(n)} = \sum_a (\bar{f}_a - f_a^{eq}) \mathcal{H}_a^{(n)}. \quad (18)$$

It is important to note here that, in [54], it is suggested to start the construction of \hat{f}_a^{neq} directly from the 2nd-order term, since the 0th-order and 1st-order terms are equal to zero by definition. However, this is true only with the explicit scheme ($\theta = 0$) for the force term in Equation (10). With the adopted semi-implicit scheme ($\theta = 0.5$), only the 0th-order expanding coefficient for \bar{f}_a^{neq} is equal to zero, i.e. $\mathbf{a}_{neq}^{(0)} = 0$ but $\mathbf{a}_{neq}^{(1)} \neq \mathbf{0}$. This is due to the existence of the force term F_a in the definition (8) of \bar{f}_a . As a consequence, the construction of \hat{f}_a^{neq} must start from the 1st-order term. In the present work, we choose to construct \hat{f}_a^{neq} up to the same order as f_a^{eq} , i.e. $N = 2$, which gives

$$\begin{aligned} \hat{f}_a^{neq} &= w_a \left(\mathbf{a}_{neq}^{(1)} \cdot \mathcal{H}_a^{(1)} + \frac{1}{2} \mathbf{a}_{neq}^{(2)} : \mathcal{H}_a^{(2)} \right), \\ &= w_a \left(\left(\sum_b (\bar{f}_b - f_b^{eq}) \frac{\boldsymbol{\xi}_b}{c_s} \right) \cdot \frac{\boldsymbol{\xi}_a}{c_s} + \frac{1}{2} \left(\sum_b (\bar{f}_b - f_b^{eq}) \left(\frac{\boldsymbol{\xi}_b \otimes \boldsymbol{\xi}_b}{c_s^2} - \mathbf{I} \right) \right) : \left(\frac{\boldsymbol{\xi}_a \otimes \boldsymbol{\xi}_a}{c_s^2} - \mathbf{I} \right) \right), \end{aligned} \quad (19)$$

where b is another lattice index.

The importance of including the 1st-order term in the regularization procedure is illustrated in Figure 1 which shows the numerical solution of a body force-driven 2D Poiseuille flow, of which the analytical solution

is $u(y) = gy(H - y)/(2\nu)$ with H being the width of the channel. In this comparison, it can be clearly observed that the regularization including both the 1st-order and 2nd-order terms gives a numerical result superimposed to the analytical solution. Whereas, the result obtained with the regularization starting directly from the 2nd-order term appears much different from the analytical solution, due to the fact that the body force effect has not been taken into account in the reconstruction of \hat{f}_a^{neq} .

Both the theoretical demonstration and the numerical example show that it is necessary to start the Hermite regularization from the 1st-order term when using the semi-implicit scheme for the force term.

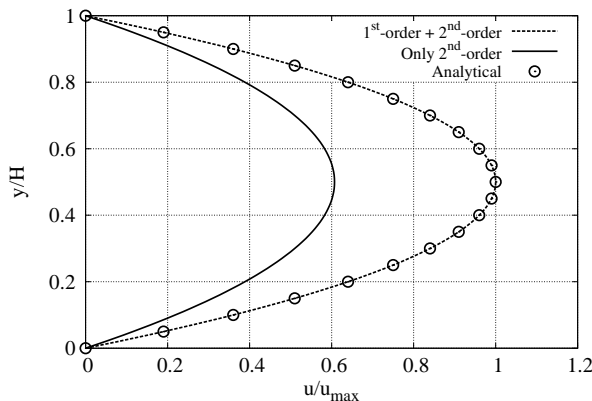


Figure 1: Numerical solution of a Poiseuille flow using the Hermite regularization procedure.

Once the non-equilibrium part $\hat{f}_a^{neq}(\mathbf{x}, t)$ is constructed by means of the regularization procedure, we can carry out the collision step in the lattice Boltzmann equation (7) as

$$\bar{f}_a(\mathbf{x} + \boldsymbol{\xi}_a \Delta t, t + \Delta t) = f_a^{eq}(\mathbf{x}, t) + \left(1 - \frac{\Delta t}{\bar{\tau}}\right) \hat{f}_a^{neq}(\mathbf{x}, t) + \Delta t \left(1 - \frac{\Delta t}{2\bar{\tau}}\right) F_a(\mathbf{x}, t), \quad (20)$$

in which the right hand side contains exclusively the expansion terms not higher than 2nd-order.

3. Direct-forcing immersed boundary method

In order to incorporate moving solid objects in fluid flows, we apply the direct-forcing immersed boundary (IB) method proposed in [32], which enhances the no-slip boundary condition on the Lagrangian solid points, thanks to the computation of a local thickness for each IB-segment as shown in Figure 2.

After each spreading step in the LB method, the distribution function $\bar{f}_a(\mathbf{x}, t)$ is updated to the time instant $t^{n+1} = t^n + \Delta t$, i.e. $\bar{f}_a^{n+1} = \bar{f}_a(\mathbf{x}, t^{n+1})$ is known everywhere inside the fluid domain, which allows us to calculate the fluid density $\rho(\mathbf{x}, t^{n+1})$. However, the macroscopic fluid velocity $\mathbf{v}(\mathbf{x}, t^{n+1})$ cannot be determined yet, since it depends not only on $\bar{f}_a(\mathbf{x}, t^{n+1})$ but also on the body force $\mathbf{F}(\mathbf{x}, t^{n+1})$, as shown in Equation (9).

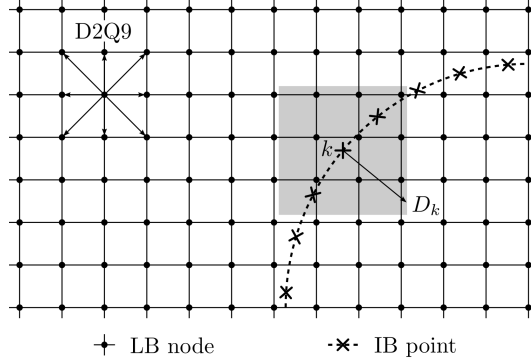


Figure 2: Immersed boundary (IB) points in a D2Q9 lattice Boltzmann (LB) grid. The shaded area represents the supporting domain D_k of the approximate Dirac delta function for the k^{th} -IB point.

Given the motion (position and velocity) of a rigid solid wall at t^{n+1} , the adopted IB method proceeds in two stages [32]:

- *Interpolation stage:* Based on the interpolated definition of the macroscopic fluid velocity, the body force on the k^{th} -IB point is computed as

$$\mathbf{F}_k^{n+1} = \frac{2}{\Delta t} \left(\mathcal{I} \left[\sum_a \bar{f}_a^{n+1} \right]_k \mathbf{v}_{s,k}^{n+1} - \mathcal{I} \left[\sum_a \bar{f}_a^{n+1} \boldsymbol{\xi}_a \right]_k \right), \quad (21)$$

where $\mathbf{F}_k^{n+1} = \mathbf{F}(\mathbf{x}_k(\mathbf{X}_k, t^{n+1}), t^{n+1})$ denotes the body force per unit volume exerted by the k^{th} -IB point at the time instant t^{n+1} , with \mathbf{x}_k and \mathbf{X}_k representing respectively the spatial and material coordinates of the k^{th} -IB point. In addition, $\mathbf{v}_{s,k}^{n+1}$ is the solid velocity at the k^{th} -IB point under the no-slip boundary condition. Finally, $\mathcal{I}[\bullet]_k$ is the interpolation operator, which gives the value of a fluid variable $\phi(\mathbf{x}, t)$ interpolated from the LB nodes to the k^{th} -IB point

$$\mathcal{I}[\phi(\mathbf{x}, t)]_k = \sum_{j \in D_k} \phi(\mathbf{x}_j, t) \tilde{\delta} \left(\frac{|x_j - x_k(t)|}{\Delta x} \right) \tilde{\delta} \left(\frac{|y_j - y_k(t)|}{\Delta y} \right), \quad (22)$$

where x_j and y_j denote the coordinates in x - and y -directions of the j^{th} -LB node that is located inside the support domain D_k of the k^{th} -IB point, as shown in Figure 2. Moreover, $\tilde{\delta}(r)$ represents an approximate Dirac delta function over the support domain D_k . In the present work, we adopt the approximate Dirac delta function proposed by Roma et al. [42]

$$\tilde{\delta}(r) = \begin{cases} \frac{1}{3} \left(1 + \sqrt{-3r^2 + 1} \right) & 0 \leq r \leq 0.5, \\ \frac{1}{6} \left[5 - 3r - \sqrt{-3(1-r)^2 + 1} \right] & 0.5 \leq r \leq 1.5, \\ 0 & \text{otherwise.} \end{cases} \quad (23)$$

- *Spreading stage:* Once the body force is obtained at all solid IB points, it is spread from the IB points onto the neighboring LB nodes by means of a spreading operation

$$\mathbf{F}(\mathbf{x}_j, t^{n+1}) = \sum_{k \in D_j} \tilde{\delta} \left(\frac{|x_j - x_k^{n+1}|}{\Delta x} \right) \tilde{\delta} \left(\frac{|y_j - y_k^{n+1}|}{\Delta y} \right) \frac{\epsilon_k^{n+1} \Delta s_k^{n+1}}{\Delta x \Delta y} \mathbf{F}_k^{n+1}, \quad (24)$$

where ϵ_k^{n+1} and Δs_k^{n+1} denote the body force at the j^{th} -LB node, the thickness and the length of the k^{th} -IB segment at the time instant t^{n+1} , respectively. More details on the computation of ϵ_k can be found in [12, 32].

Using the newly obtained body force $\mathbf{F}(\mathbf{x}, t^{n+1})$, we can calculate the macroscopic fluid velocity $\mathbf{v}(\mathbf{x}, t^{n+1})$ defined in Equation (9), the equilibrium distribution function $f_a^{eq}(\mathbf{x}, t^{n+1})$ with Equation (2) and the body force term $F_a(\mathbf{x}, t^{n+1})$ with Equation (4), so that we can proceed the collision step for the next time-step.

4. Non-staggered IB-RLB coupling for FSI

4.1. Equation of rigid solid motion

The dynamical equilibrium equation for an elastically mounted rigid solid object with two degrees of freedom can be written as

$$M_s \mathbf{a}_s(t) + C_s \mathbf{v}_s(t) + K_s \mathbf{u}_s(t) = \mathcal{F}(t), \quad (25)$$

where $\mathbf{u}_s(t)$, $\mathbf{v}_s(t)$ and $\mathbf{a}_s(t)$ are the displacement, velocity and acceleration of the solid body in x - and y -directions. M_s , C_s and K_s denote respectively the mass, the damping coefficient and the stiffness of this mass-spring system. $\mathcal{F}(t)$ is the total force exerted from the surrounding fluid flow to the solid cylinder.

By integrating Equation (25) in time with the explicit Newmark scheme [37], we obtain

$$\left\{ \begin{array}{l} \left(\frac{2M_s}{\Delta t} + C_s \right) \mathbf{v}_s^{n+1} - \mathcal{F}^{n+1} = \frac{2M_s}{\Delta t} \left(\mathbf{v}_s^n + \frac{\Delta t}{2} \mathbf{a}_s^n \right) - K_s \left(\mathbf{u}_s^n + \Delta t \mathbf{v}_s^n + \frac{\Delta t^2}{2} \mathbf{a}_s^n \right), \\ \mathbf{u}_s^{n+1} = \mathbf{u}_s^n + \Delta t \mathbf{v}_s^n + \frac{\Delta t^2}{2} \mathbf{a}_s^n, \\ \mathbf{v}_s^{n+1} = \mathbf{v}_s^n + \frac{\Delta t}{2} (\mathbf{a}_s^{n+1} + \mathbf{a}_s^n), \end{array} \right. \quad (26)$$

where $\mathbf{u}_s^{n+1} = \mathbf{u}_s(t^{n+1})$, $\mathbf{v}_s^{n+1} = \mathbf{v}_s(t^{n+1})$ and $\mathbf{a}_s^{n+1} = \mathbf{a}_s(t^{n+1})$ denote the displacement, velocity and acceleration of the solid body at the instant t^{n+1} with $\Delta t = t^{n+1} - t^n$.

4.2. Coupling strategy

As shown in Equation (26), without knowing \mathcal{F}^{n+1} , one cannot update the solid state to $t = t^{n+1}$ to obtain \mathbf{u}_s^{n+1} , \mathbf{v}_s^{n+1} and \mathbf{a}_s^{n+1} . In this situation, in a staggered coupling algorithm [24], it is assumed that $\mathcal{F}^{n+1} \simeq \mathcal{F}^n$ with \mathcal{F}^n being already known from the previous time-step, or $\mathcal{F}^{n+1} \simeq \mathcal{F}^p$ with \mathcal{F}^p denoting a predicted force.

The drawback of staggered coupling methods is that the time-lag between the two sub-domains (fluid and solid) might sometimes induce numerical instabilities, even though each individual sub-domain is numerically stable. Using sub-iterations within each physical time-step may reduce the time-lag, however this leads to low numerical efficiency, due to the extra sub-iterations, which may even lead to difficulties in converging for strongly coupled FSI problems [19].

Inspired by the work in [31], we employ a non-staggered coupling strategy to solve this FSI problem. The key is to obtain an equation relating the solid velocity \mathbf{v}_s^{n+1} and the total force \mathcal{F}^{n+1} with the help of the IB method. Given the body force per unit volume at the k^{th} -IB segment in Equation (21), the total force \mathcal{F}^{n+1} can be computed as

$$\begin{aligned}\mathcal{F}^{n+1} &= -\sum_k \epsilon_k^{n+1} \Delta s_k^{n+1} \mathbf{F}_k^{n+1}, \\ &= -\frac{2}{\Delta t} \sum_k \epsilon_k^{n+1} \Delta s_k^{n+1} \left(\mathcal{I} \left[\sum_a \bar{f}_a^{n+1} \right]_k \mathbf{v}_{s,k}^{n+1} - \mathcal{I} \left[\sum_a \bar{f}_a^{n+1} \boldsymbol{\xi}_a \right]_k \right).\end{aligned}\quad (27)$$

In the present case, because the rigid cylinder is allowed to move in x - and y -directions without rotation, all the IB points have the same velocity, i.e. $\mathbf{v}_{s,k}^{n+1} = \mathbf{v}_s^{n+1}$, where $\forall k \in [1, N_s]$ with N_s being the total number of the IB points. As a consequence, Equation (27) can be rewritten as

$$\left(\frac{2}{\Delta t} \sum_k \epsilon_k^{n+1} \Delta s_k^{n+1} \mathcal{I} \left[\sum_a \bar{f}_a^{n+1} \right]_k \right) \mathbf{v}_s^{n+1} + \mathcal{F}^{n+1} = \frac{2}{\Delta t} \sum_k \epsilon_k^{n+1} \Delta s_k^{n+1} \mathcal{I} \left[\sum_a \bar{f}_a^{n+1} \boldsymbol{\xi}_a \right]_k, \quad (28)$$

where one should note that only \mathbf{v}_s^{n+1} and \mathcal{F}^{n+1} are unknowns, since \bar{f}_a^{n+1} is obtained from the streaming step of LB method, and ϵ_k^{n+1} and Δs_k^{n+1} depend on the new solid position \mathbf{u}_s^{n+1} or geometry that has been updated by means of the explicit Newmark time integrator using the second equation in the system (26).

Regrouping the first equation in the system (26) and Equation (28) gives

$$\begin{bmatrix} \mathcal{K}_s & -1 \\ \mathcal{K}_f & 1 \end{bmatrix} \begin{bmatrix} \mathbf{v}_s^{n+1} \\ \mathcal{F}^{n+1} \end{bmatrix} = \begin{bmatrix} \mathbf{g}_s \\ \mathbf{g}_f \end{bmatrix}, \quad (29)$$

where \mathcal{K}_s , \mathcal{K}_f , \mathbf{g}_s and \mathbf{g}_f are all known before solving the system (29) due to use of the explicit Newmark scheme for the solid, which are

$$\begin{cases} \mathcal{K}_s = \frac{2M_s}{\Delta t} + C_s, \\ \mathcal{K}_f = \frac{2}{\Delta t} \sum_k \epsilon_k^{n+1} \Delta s_k^{n+1} \mathcal{I} \left[\sum_a \bar{f}_a^{n+1} \right]_k, \\ \mathbf{g}_s = \frac{2M_s}{\Delta t} \left(\mathbf{v}_s^n + \frac{\Delta t}{2} \mathbf{a}_s^n \right) - K_s \left(\mathbf{u}_s^n + \Delta t \mathbf{v}_s^n + \frac{\Delta t^2}{2} \mathbf{a}_s^n \right), \\ \mathbf{g}_f = \frac{2}{\Delta t} \sum_k \epsilon_k^{n+1} \Delta s_k^{n+1} \mathcal{I} \left[\sum_a \bar{f}_a^{n+1} \boldsymbol{\xi}_a \right]_k. \end{cases} \quad (30)$$

Now, \mathbf{v}_s^{n+1} and \mathcal{F}^{n+1} can be simultaneously obtained by solving the system of equations (29) without any sub-iteration procedure during each physical time-step from t^n to t^{n+1} . We can then use \mathbf{v}_s^{n+1} to get \mathbf{F}_k^{n+1} by Equation (21), and thus $\mathbf{F}(\mathbf{x}_j, t^{n+1})$ by Equation (24).

4.3. Overview of the present IB-RLB coupling algorithm

The present IB-RLB coupling algorithm can be summarized as follows:

Algorithm 1: IB-RLB coupling algorithm

Require: $\bar{f}_a(\mathbf{x}, t^n)$, $\rho(\mathbf{x}, t^n)$, $\mathbf{v}(\mathbf{x}, t^n)$ and $\mathbf{F}(\mathbf{x}, t^n)$ from the previous time-step

- 1: Compute $f_a^{eq}(\mathbf{x}, t^n)$ with Equation (2) and $F_a(\mathbf{x}, t^n)$ with Equation (4)
- 2: Extract $\bar{f}_a^{neq}(\mathbf{x}, t^n)$ by Equation (16)
- 3: Compute $\mathbf{a}_{neq}^{(1)}(\mathbf{x}, t^n)$ and $\mathbf{a}_{neq}^{(2)}(\mathbf{x}, t^n)$ with Equation (18)
- 4: Obtain $\hat{f}_a^{neq}(\mathbf{x}, t^n)$ using Equation (19)
- 5: Regularized LB-collision step in Equation (20)
- 6: Obtain $\bar{f}_a(\mathbf{x}, t^{n+1})$ by means of LB-streaming step and thus $\rho(\mathbf{x}, t^{n+1}) = \sum_a \bar{f}_a(\mathbf{x}, t^{n+1})$
- 7: Compute $\mathbf{u}_s^{n+1} = \mathbf{u}_s^n + \Delta t \mathbf{v}_s^n + 0.5 \Delta t^2 \mathbf{a}_s^n$ as shown in Equation (26)
- 8: Update the solid geometry and then compute ϵ_k^{n+1} using the method presented in [32]
- 9: IB-interpolation stage to get $\mathcal{I}[\sum_a \bar{f}_a^{n+1}]_k$ and $\mathcal{I}[\sum_a \bar{f}_a^{n+1} \boldsymbol{\xi}_a]_k$
- 10: Solve the equations (26) and (28) to obtain \mathbf{v}_s^{n+1} and then \mathbf{a}_s^{n+1}
- 11: Compute \mathbf{F}_k^{n+1} by Equation (21) using $\mathbf{v}_{k,s}^{n+1} = \mathbf{v}_s^{n+1}$
- 12: IB-spreading stage to obtain $\mathbf{F}(\mathbf{x}, t^{n+1})$ at each LB node by Equation (24)
- 13: Compute $\mathbf{v}(\mathbf{x}, t^{n+1})$ by the definition (9)
- 14: Goto 1 for next time-step

5. Numerical results and discussions

5.1. Taylor-Green vortex

The objective of this test-case is to verify numerically that the adopted regularization procedure does not affect the convergence order of the LB method. We consider the Taylor-Green vortex in a square domain

$[0, L] \times [0, L]$ with periodic boundary conditions, of which the analytical solution is given as

$$\begin{cases} v_x(x, y, t) = -U_0 \cos(kx) \sin(ky) e^{-2k^2 \nu t}, \\ v_y(x, y, t) = U_0 \sin(kx) \cos(ky) e^{-2k^2 \nu t}, \\ p(x, y, t) = p_0 \left(1 - \frac{U_0^2}{4c_s^2} (\cos(2kx) + \cos(2ky)) e^{-4k^2 \nu t} \right), \end{cases} \quad (31)$$

where v_x and v_y denote the velocity components in x - and y -directions, $p = \rho c_s^2$ is the pressure, U_0 and p_0 are the characteristic velocity and pressure, $k = 2\pi/L$ and $\nu = U_0 L / Re$ the kinematic viscosity with the Reynolds number chosen as $Re = 100$ in this test-case. The total time is set as $T = L/U_0$.

To evaluate the convergence order, we measure the errors of the velocity fields obtained using four lattice resolutions $N_x \times N_y = 65 \times 65, 129 \times 129, 257 \times 257$ and 513×513 , with N_x and N_y denoting respectively the number of discretization points in x - and y -directions. For all four lattice resolutions, the relaxation time is fixed at $\bar{\tau}/\Delta t = 0.596$. The error is evaluated as

$$\text{Error} = \sqrt{\frac{1}{N_x N_y} \sum_j \frac{|\mathbf{v}_j^{\text{num}} - \mathbf{v}_j^{\text{ana}}|^2}{U_0^2}}, \quad (32)$$

where $\mathbf{v}_j^{\text{num}} = \mathbf{v}^{\text{num}}(\mathbf{x}_j, T)$ and $\mathbf{v}_j^{\text{ana}} = \mathbf{v}^{\text{ana}}(\mathbf{x}_j, T)$ denote the numerical and analytical velocity vector at the j^{th} -node and the final instant $t = T$. The numerical results are obtained with the standard LB (SLB) and the regularized LB (RLB) methods for comparison.

Table 1 gives the numerical errors for different mesh resolutions and the CPU times consumed by the SLB and RLB methods, in which the CPU times are all relative to the first (65×65) SLB result. We find that the RLB method gives a slightly smaller error than the SLB method, although the RLB method is computationally more demanding than the SLB method. Based on these data in Table 1, Figure 3 shows the convergence order of the SLB and RLB methods. We observe that both the SLB and RLB methods exhibit 2nd-order convergence, which means that the regularization procedure does not degrade the convergence order of the LB method.

Table 1: Numerical errors in the Taylor-Green vortex test-case at $Re = 100$ with $\bar{\tau}/\Delta t = 0.596$.

Mesh size	Error		Relative CPU time	
	SLB	RLB	SLB	RLB
65×65	3.1473×10^{-4}	2.9025×10^{-4}	1.0	1.5
129×129	7.8366×10^{-5}	7.1902×10^{-5}	13.4	21.4
257×257	2.0171×10^{-5}	1.8588×10^{-5}	253.8	394.2
513×513	4.9317×10^{-6}	4.5245×10^{-6}	3618.2	5812.1

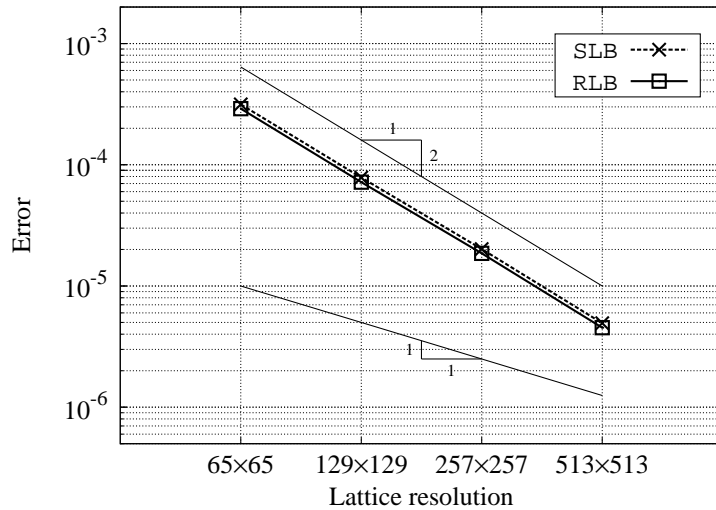


Figure 3: Convergence order of the SLB and RLB methods in the Taylor-Green vortex test-case.

5.2. Impulsively started plate

In this test-case, we consider a two-dimensional infinitely thin rigid plate of height h , which is suddenly accelerated from rest to a constant velocity U_0 in the direction normal to the plate surface. Initially, the surrounding fluid is also at rest. The Reynolds number is fixed at $Re = U_0 h / \nu = 1000$. This test-case is used in [32] for validating the IB-SLB coupling method in which the standard BGK collision model is used. Despite the good agreements with the references, it is observed that some spurious noise is generated around the slender solid object, as shown in Figure 5-(a) in [32].

In the present numerical simulation using the proposed IB-RLB coupling method, the size of the fluid domain is set as $15h \times 9h$ and the rigid plate is discretized with 64 segments of the same length ($\Delta s = \Delta x = \Delta y$). The vorticity contour lines are shown in Figure 4 at four different instants ($t^* = tU_0/h = 0.1, 0.5, 1.0$ and 2.0), which are compared with ones obtained with the previous IB-SLB coupling method [32]. Since the fluid flow is symmetric with respect to the central line, the upper half and lower half of each sub-figure drawn in Figure 4 show the vorticity contour lines obtained with the IB-SLB and IB-RLB models, respectively. It can be observed that due to the sudden presence of the moving solid boundary, some spurious noise appears in the vorticity field obtained with the IB-SLB method, whereas the IB-RLB method provides a much smoother vorticity field, especially at time $t^* = 0.1$ as shown in Figure 4-(a). As time evolves, the results of the IB-SLB and IB-RLB methods become very close to each other. In addition, Figure 5 shows the time evolution of the dimensionless length s/h of the recirculation pocket behind the moving plate, of which the shape is determined by the contour line for $v_x = U_0$. In this comparison one can observe that the results given by the IB-SLB and IB-RLB methods

are both in good agreement with the reference.

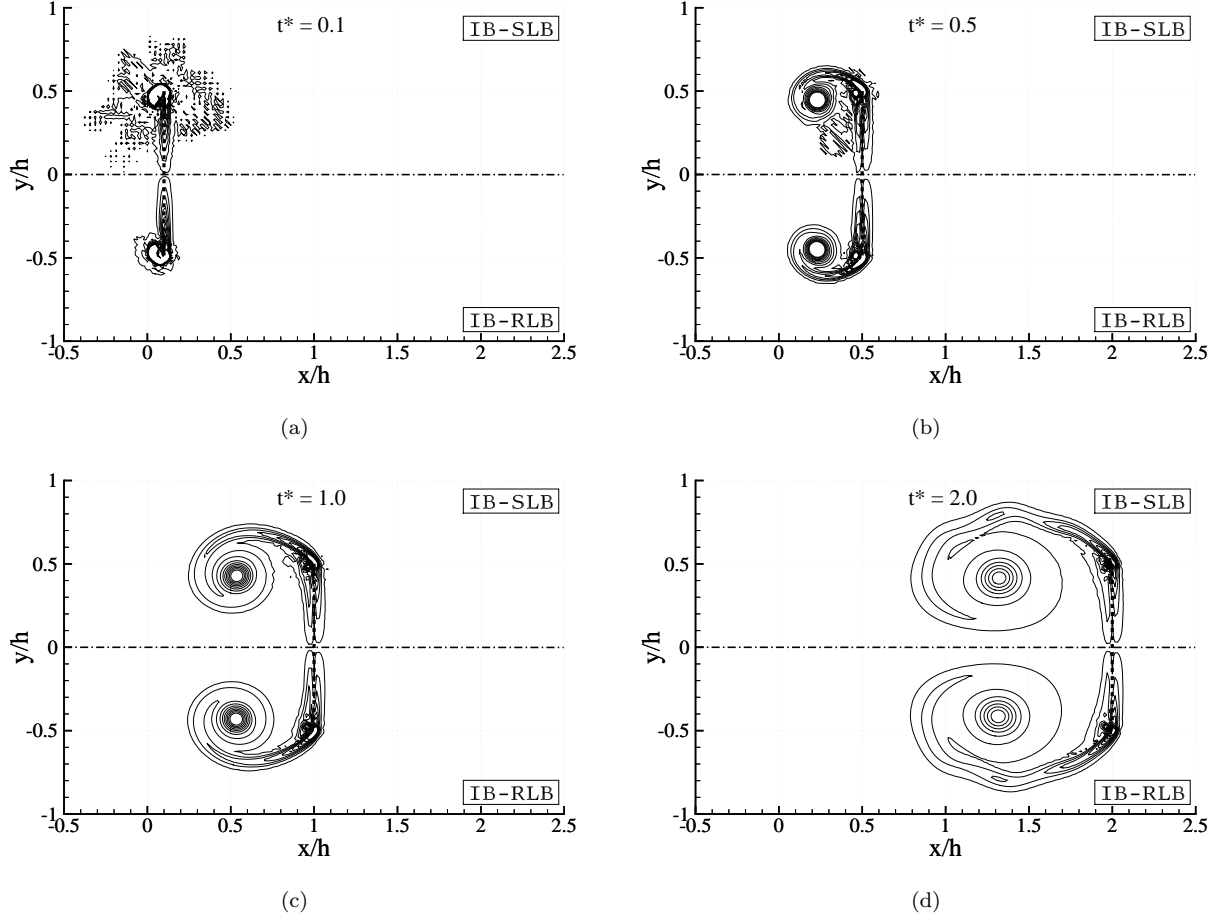


Figure 4: Vorticity contour lines in the impulsively started plate test-case at four instants ($t^* = tU_0/h = 0.1, 0.5, 1.0$ and 2.0).

Hence, the adopted regularization procedure in the proposed IB-RLB coupling method can efficiently reduce undesired noises, as shown in Figure 4-(a) and (b).

5.3. Vortex-induced vibrations (VIV)

In this part the proposed IB-RLB coupling method is validated with a series of two-way FSI test-cases, in which an elastically mounted circular cylinder is allowed to move in either only y -direction or both x - and y -directions, while interacting with a uniform fluid flow in x -direction. Figure 6 shows the configuration of these test-cases. A rigid cylinder of diameter D is mounted on an elastic support and initially placed on the horizontal central line of the computational fluid domain of height H . The distance from the cylinder to the upstream (inlet) and downstream (outlet) boundaries are noted as L_u and L_d , respectively.

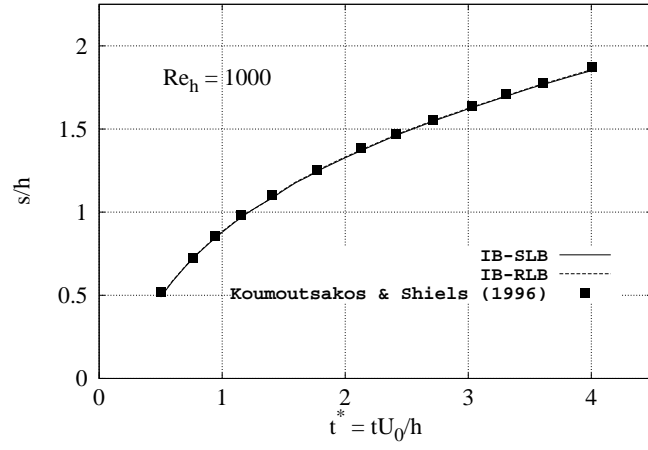


Figure 5: Time evolution of the length of the recirculation bubble.

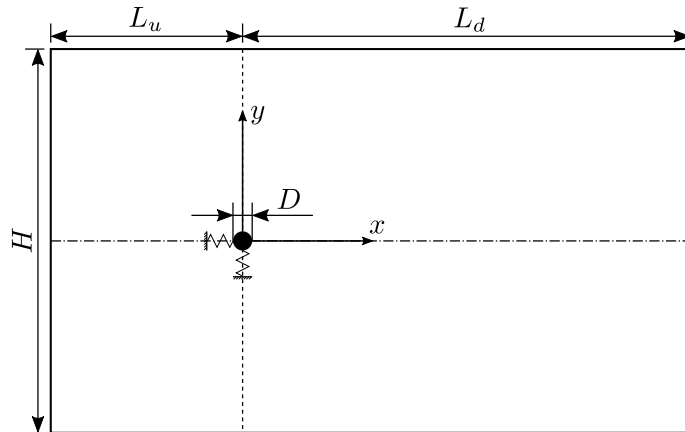


Figure 6: Configuration of the VIV test-cases.

The boundary conditions are the same as the ones used by Prasanth and Mittal [39]. A velocity boundary condition is imposed at the inlet: $v_x(-L_u, y, t) = U_0$ and $v_y(-L_u, y, t) = 0$. At the outlet, the pressure or density is fixed at the reference value: $\rho(L_d, y, t) = \rho_0$. On the two lateral sides, we impose that $v_y(x, y_B, t) = 0$ and $\partial v_x / \partial y(x, y_B, t) = 0$ with y_B being equal to $\pm H/2$.

Moreover, in order to compare with other results in the literature, we choose to adopt the same size of the computational domain as the one used in [17, 44], which gives $H = 20D$, $L_u = 10D$ and $L_d = 25.5D$.

5.3.1. Flow past a fixed circular cylinder at $Re = 100$ and $Re = 185$

Before considering two-way FSI problems, we first validate the present IB-RLB coupling method by means of a test-case in which the cylinder is fixed in the surrounding fluid flow at $Re = U_0 D / \nu = 100$. Table 2 shows the numerical results of the averaged drag coefficient $\text{avg}(C_D)$, the root mean square of the lift coefficient $\text{rms}(C_L)$, the amplitude of the lift coefficient $\text{amp}(C_L)$ and the Strouhal number $St = f_s D / U_0$ with f_s being the vortex shedding frequency, which are compared with references of the literature. A good agreement can be found in this comparison and we observe that the lattice size with $D = 40\Delta x$ provides a reasonably accurate solution. In the following test-cases, we use this lattice resolution to validate the proposed IB-RLB coupling method in a series of two-way FSI problems.

Table 2: Numerical results of the fluid flow past a fixed cylinder at $Re = 100$.

References	$\text{avg}(C_D)$	$\text{rms}(C_L)$	$\text{amp}(C_L)$	St	
Present	$D = 40\Delta x$	1.415	0.252	0.356	0.169
	$D = 80\Delta x$	1.404	0.249	0.352	0.168
	$D = 120\Delta x$	1.400	0.247	0.350	0.169
Zhang et al. [53]	1.425	0.250	–	0.173	
Singh and Mittal [44]	1.310	0.250	–	0.163	
He et al. [17]	1.377	0.251	0.355	0.169	
Yang et al. [52]	1.393	–	0.335	0.165	

Next, we consider a slightly higher Reynolds number $Re = U_0 D / \nu = 185$, at which the fluid flow is still two-dimensional and laminar. In LB simulations, in order to increase the Reynolds number, one can use a greater characteristic velocity U_0 , or an increased diameter D of the cylinder, or a smaller viscosity ν leading to a relaxation time $\bar{\tau} / \Delta t$ closer to 0.5. However, there exist some limitations: (i) U_0 has to be kept small enough comparing to the lattice speed of sound c_s , because of the weakly-compressible hypothesis; (ii) a greater $D / \Delta x$ usually means a larger number of discretization points demanding more computational resources, which is not always necessary, especially for fluid flows at low Re numbers; (iii) it is well known that when $\bar{\tau} / \Delta t$ becomes too close to 0.5, LB simulations often encounter numerical instabilities, even at low Re numbers.

In the present study, we increase the Reynolds number to $Re = U_0 D / \nu = 185$ by only decreasing the kinematic viscosity ν , while keeping the diameter of the cylinder $D/\Delta x = 40$ and the inlet velocity $U_0/c_s = 0.05/(1/\sqrt{3}) \simeq 0.0866$. This gives a relaxation time $\bar{\tau}/\Delta t \simeq 0.5324$. Table 3 shows the numerical results obtained with the proposed IB-RLB coupling method, in which a good agreement can be found with the references.

Table 3: Numerical results of the fluid flow past a fixed cylinder at $Re = 185$.

		avg(C_D)	rms(C_L)	St
Present	$D = 40\Delta x$	1.400	0.479	0.197
Vanella and Balaras [48]		1.377	0.461	–
Pinelli et al. [38]		1.430	0.423	0.196

It is here worth noting that the standard SRT-BGK model (IB-SLB coupling method) cannot provide a stable numerical simulation at $Re = 185$ using the same parameters, i.e. with the same U_0 , D and $\bar{\tau}$ as previously presented. A possible way to remedy the situation is to refine the lattice so that $D/\Delta x$ is greater, which is, of course, computationally more costly. This test-case shows clearly the importance of the regularization procedure based on the Hermite expansion.

5.3.2. Flow past a y -oscillating cylinder

In this test-case, the cylinder is attached to a mass-spring system and allowed to oscillate transversely in y -direction. We adopt the same physical parameters as the ones used in [10, 17], which lead to the following dimensionless numbers: the mass ratio $m^* = 4M_s/(\rho_0\pi D^2) \simeq 149.1$, the damping ratio $\zeta = C_s/(2\sqrt{M_s K_s}) = 0.001237$ and the Reynolds number $Re = U_0 D / \nu$ varies from $Re = 90$ to $Re = 120$, corresponding to reduced velocities $U^* = U_0/(f_n D)$ from $U^* = 5.01$ to $U^* = 6.68$, where $f_n = \sqrt{K_s/M_s}/(2\pi)$ denotes the natural vibration frequency of the mass-spring system. Notice that all the following cases with different Re or U^* are carried out separately, starting from the stabilized fixed cylinder result. Hence, no hysteresis phenomenon is considered.

Figure 7 shows the time-varying positions of the center of the oscillating cylinder at $Re = 90, 100$ and 120 , corresponding to $U^* = 5.01, 5.57$ and 6.68 , respectively. In addition, the instantaneous vorticity contours in the wake of the oscillating cylinder are also provided in Figure 7. By plotting the maximal amplitude and the frequency of the oscillation as functions of Reynolds number Re , as shown in Figure 8, one can easily observe the *lock-in* phenomenon [7, 50] in this VIV problem. As Re increases, from a critical value ($Re \simeq 96$), the maximal amplitude of the oscillation A_{max} suddenly has a significant value. After that, A_{max} slightly decreases when increasing Re . When Re becomes greater than a second critical value ($Re \simeq 110$), A_{max} quickly falls to a small value and remains close to zero, as Re keeps increasing. Meanwhile, the vibration frequency f_v of the

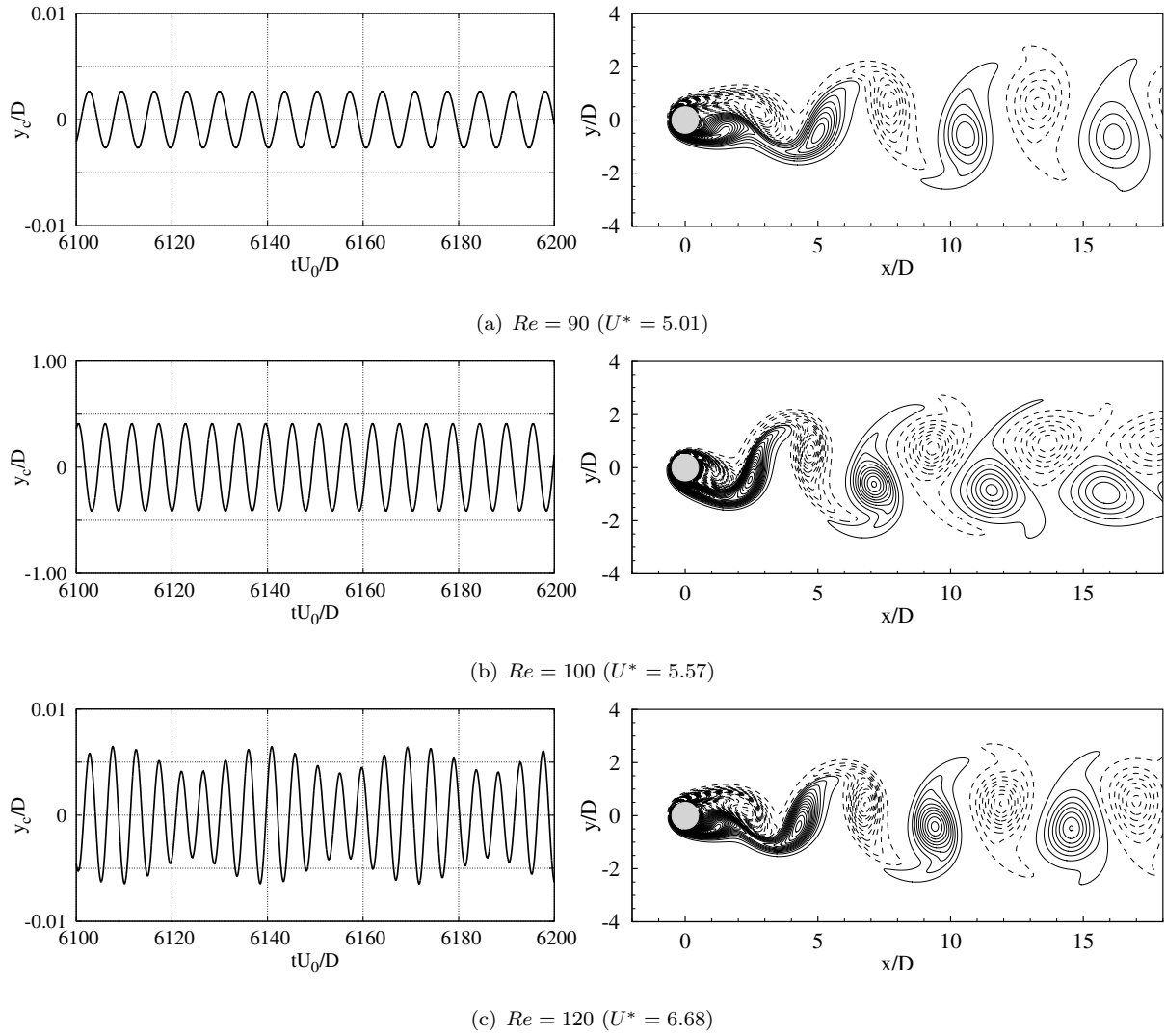


Figure 7: The position of the center of the y -oscillating cylinder and the vorticity contour lines at three different Re values.

cylinder continuously increases but remains constant ($f_v/f_n \simeq 1$) between the two critical Reynolds numbers ($96 \leq Re \leq 110$).

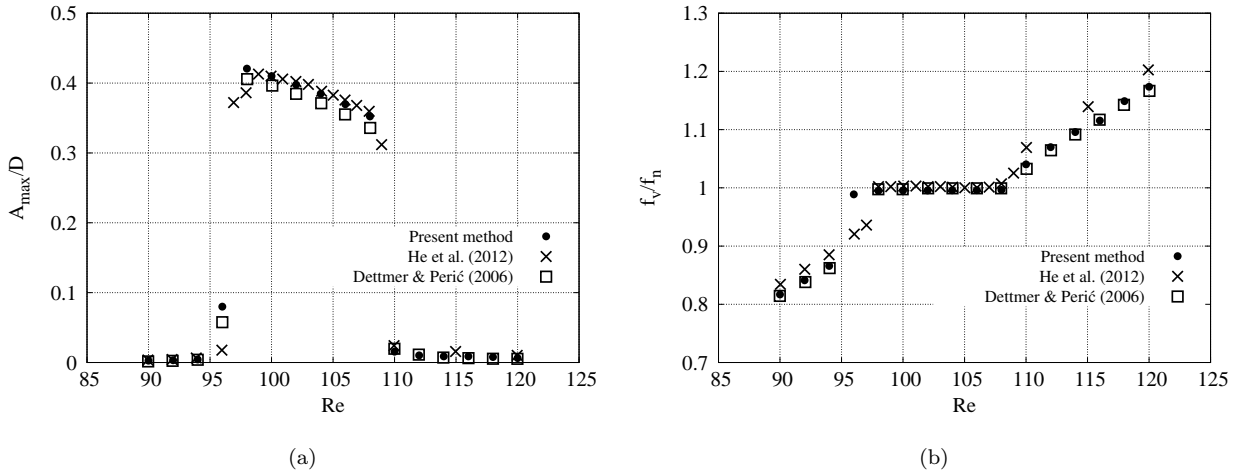


Figure 8: Lock-in phenomenon in the y-oscillating cylinder test-case.

As shown in the comparison with the references [10, 17] in Figure 8, the proposed IB-RLB coupling method can correctly capture the frequency lock-in regime in this VIV problem. The critical Reynolds numbers and the maximal vibration amplitude are in good agreement with the references which, based on ALE finite element formulations using body-fitted meshes, adopt a monolithic coupling strategy (Dettmer & Perić [10]) and use a loosely-coupled partitioned coupling method (He et al. [17]).

5.3.3. Flow past an xy -oscillating cylinder

Now, the cylinder is allowed to oscillate in both x - and y -directions. The mass-spring system has the same properties in both directions. The dimensionless numbers are set as [44, 49]: $Re = 100$, $m^* = 10$, $\zeta = 0$ and $U^* = 4.0 - 8.0$. In the present study, we observe that it is necessary to increase the upstream distance to $L_u = 15D$ in order to eliminate the interference with the inlet boundary.

Figure 9 shows the trajectories of the cylinder center and the maximal oscillation amplitudes at different reduced velocities U^* . Eight-shaped trajectories are obtained at reduced velocities $U^* = 5.0, 6.0$ and 7.0 , which are very close to the ones presented in [49]. In addition, a good agreement is found with the references [44, 49] for the maximal oscillation amplitude A_y^{max} in y -direction within the interval of reduced velocity $U^* \in [4.0, 8.0]$.

5.4. Fluid-deformable structure interaction in a 2D flow channel

Previously, we validated the proposed IB-RLB coupling method by means of several FSI test-cases, in which only rigid solid bodies were considered. The present test-case is the widely adopted (see, e.g., recent works

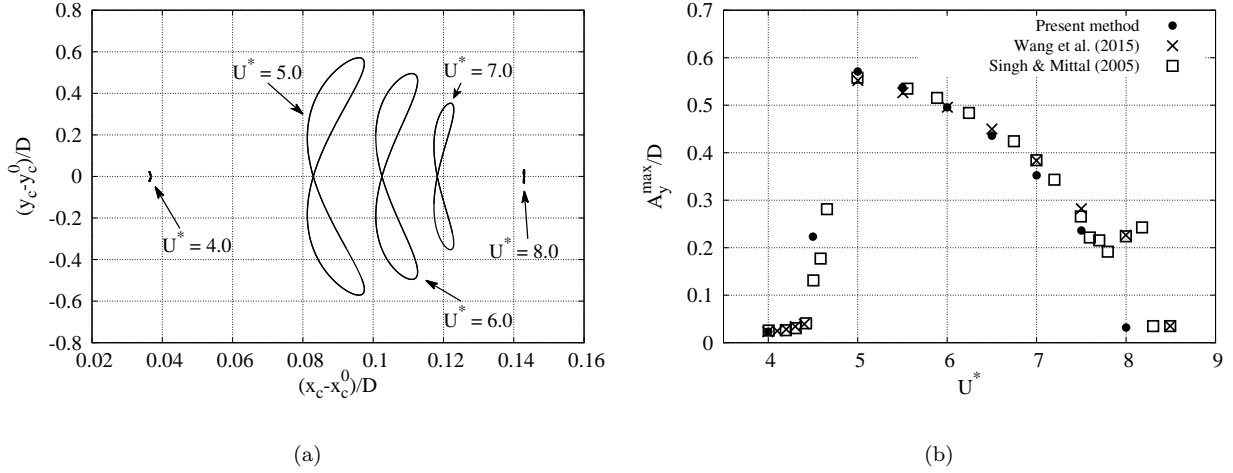


Figure 9: The xy-oscillating cylinder test-case (left: trajectories of the cylinder center at different reduced velocities; right: maximum amplitudes in y -direction).

in [11, 23, 31]) benchmarking FSI problem in the presence of a deformable elastic solid structure, which was initially proposed by Turek and Hron [47]. Figure 10 shows the configuration of this test-case: a deformable solid bar, simulated by finite element method (FEM), is attached in the wake of a rigid cylinder in a 2D flow channel at $Re = 100$ (FSI2) and $Re = 200$ (FSI3). The geometric, material and discretization parameters are shown in Table 4. Here, the Hermite expansion-based regularization procedure for the LBM is expected to improve the numerical stability in the FE-LB coupling framework [31]. Thus, the objective of this test-case is to further validate the proposed IB-RLB coupling method in such a FSI problem with a deformable solid structure. More details on the adopted FE-LB coupling scheme can be found in [31].

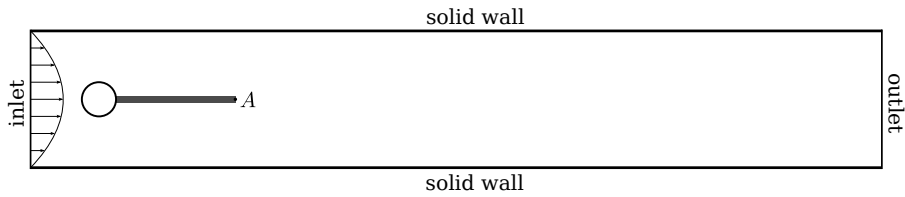


Figure 10: Configuration of the fluid-deformable structure interaction (FSI2 and FSI3 [47]) test-cases.

Figure 11 gives the time history of the vertical displacement of the point A (see Figure 10) in the FSI2 test-case, which is compared with the one obtained with the previous IB-SLB method using standard BGK collision model. We observe that the results of IB-SLB and IB-RLB methods are very close to each other, which are both in good agreement with the reference [47]. Moreover, snapshots of the pressure field and streamlines at four instants are shown in Figure 12, corresponding to four different positions of the point A.

Table 4: [Geometric, material and discretization parameters in the fluid-deformable structure interaction test-case.](#)

	$Re = 100$	$Re = 200$
Length of the flow channel	2.5 m	2.5 m
Height of the flow channel	0.41 m	0.41 m
Radius of the fixed cylinder	0.05 m	0.05 m
Length of the deformable solid bar	0.35 m	0.35 m
Thickness of the solid bar	0.02 m	0.02 m
Initial fluid density	10^3 kg/m^3	10^3 kg/m^3
Fluid kinematic viscosity	$10^{-3} \text{ m}^2/\text{s}$	$10^{-3} \text{ m}^2/\text{s}$
Initial solid density	10^4 kg/m^3	10^3 kg/m^3
Solid Poisson ratio	0.4	0.4
Solid Young's modulus	$1.4 \times 10^6 \text{ Pa}$	$5.6 \times 10^6 \text{ Pa}$
Mean incoming fluid velocity	1 m/s	2 m/s
Solid-to-fluid density ratio	10	1
Grid spacing	$2 \times 10^{-3} \text{ m}$	$2 \times 10^{-3} \text{ m}$
Time-step	10^{-4} s	$1.6 \times 10^{-5} \text{ s}$

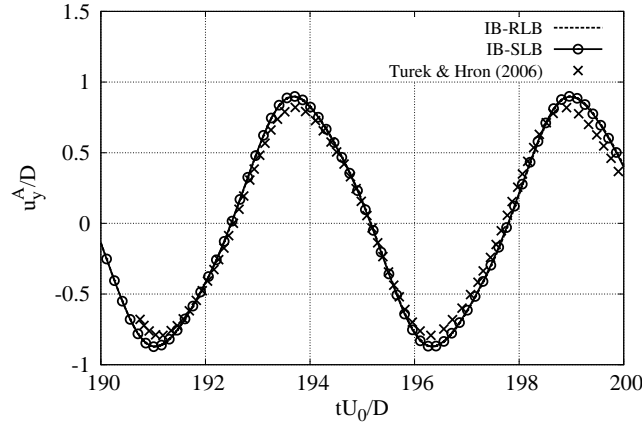


Figure 11: Evolution in time of the vertical displacement of the point A in the FSI2 test-case.

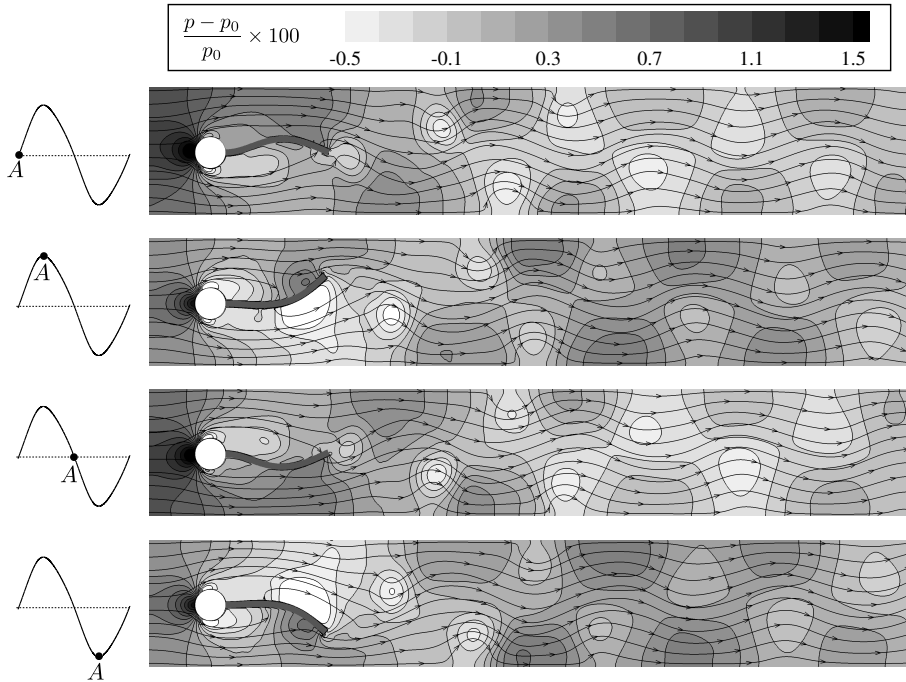


Figure 12: Pressure fields and streamlines at four instants in the fluid-deformable structure interaction (FSI2) test-case.

Next, we consider the FSI3 test-case having a higher Reynolds number $Re = 200$ than in the FSI2. As shown in Table 4, in this case the solid-to-fluid density ratio is equal to 1, which is more challenging than the previous case, as the FSI effects become more important. Additionally, the time-step is decreased to $\Delta t = 1.6 \times 10^{-5}$ s, which is due to the increased sound speed in the solid structure and the use of the explicit Newmark time integrator in the FE solver. We carried out the simulations with the previous IB-SLB [31] and the present IB-RLB coupling methods and we observed that the IB-SLB method failed to provide a stable simulation. The FSI simulation diverged quickly after several hundred time-steps. We found that with the parameters in Table 4, the value of $\bar{\tau}/\Delta t$ is equal to 0.512, which is too close to 0.5 for the SRT-LBM. Numerical instabilities developed in the LBM simulation and finally affected the numerical stability of the IB-SLB coupling. As expected, the Hermite expansion-based regularization procedure succeeded in improving the numerical stability of the IB-RLB coupling with the same parameters as in the IB-SLB one. Figure 13 shows the vertical displacement of the point A , as time evolves. In addition, the oscillation amplitude $A_m = (\max(u_y^A) - \min(u_y^A))/2$, the Strouhal number $St = f_A D/U_0$ with f_A being the oscillation frequency, and the averaged drag coefficient $\text{avg}(C_D)$ are given in Table 5, in which one may observe that the present results qualitatively agree with the references.

It is here worth noting that the previous IB-SLB may be stable with a $\bar{\tau}/\Delta t$ much greater than 0.5. However, this requires a higher lattice resolution, as discussed previously in Section 5.3.1. In future works, the present

IB-RLB coupling method may be tested with some more challenging problems with very small solid-to-fluid density/mass ratios such as the ones adopted in [13, 51].

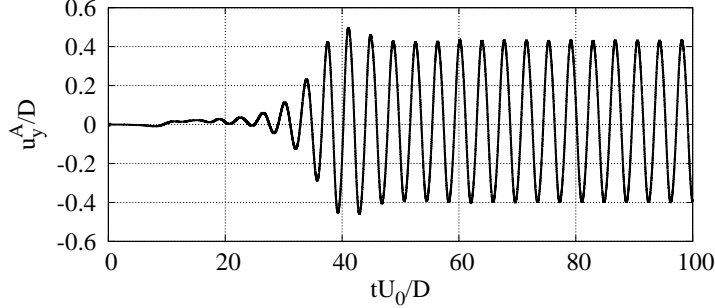


Figure 13: Evolution in time of the vertical displacement of the point A in the FSI3 test-case at $Re = 200$.

Table 5: Numerical results in the fluid-deformable structure interaction test-case FSI3 at $Re = 200$.

	A_m/D	St	$\text{avg}(C_D)$
Present IB-RLB	0.41	0.26	2.43
Tian et al. (2014) [46]	0.32	0.29	2.16
Bhardwaj and Mittal (2012) [2]	0.41	0.28	2.20
Turek and Hron (2006) [47]	0.36	0.26	2.30

5.5. 3D flapping flag in a uniform flow

At last, we consider a 3D test-case involving the interaction between an elastic flag and a uniform incoming fluid flow. Figure 14 shows the initial configuration, where a square flag of length L is set in a fluid domain of size $[-L, 7L] \times [-4L, 4L] \times [-L, L]$, in x -, y - and z -directions, respectively. The flag is fixed at its leading edge, of which the center O is the origin of the coordinate system. Initially, the flag is held at an angle of $\theta = 0.1\pi$ from the x - z plane. At the inlet ($x = -L$) as well as the far-field boundaries ($y = \pm 4L$) of the fluid domain, a uniform velocity condition is imposed as $v_x = U_0$ and $v_y = v_z = 0$. Periodic boundary condition is applied at the lateral surfaces in the spanwise (z) direction. At the outlet, the pressure is fixed at p_0 and the zero-gradient condition is imposed for all velocity components.

This 3D flapping flag test-case, initially conducted by Huang and Sung [21], has been widely adopted in several recent works [8, 11, 29, 46] for validating different numerical methods. In the present work, we first consider the case with a Reynolds number $Re = U_0 L / \nu = 200$. The mass ratio is chosen as $\rho_s h / (\rho_f L) = 1$, where ρ_s and ρ_f denote the solid and fluid densities, respectively. In addition, as did in [46], the thickness

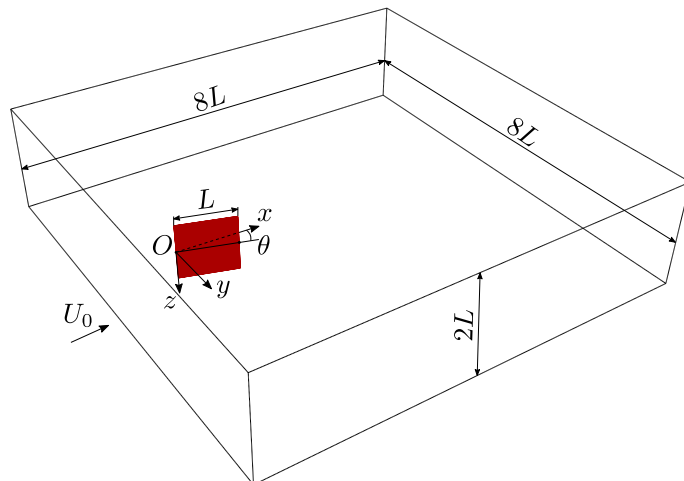


Figure 14: Initial configuration of the 3D flapping flag test-case.

of the flag is set as $h = 0.01L$ in the present 3D volumetric finite element modeling. For the solid structure, the Poisson's ratio is $\nu_s = 0.4$ and the Young modulus E_s is chosen such that the bending rigidity is equal to $E_s h^3 / (12(1 - \nu_s^2) \rho_f U_0^2 L^3) = 0.0001$.

The fluid computational domain is discretized using a uniform grid of size $401 \times 401 \times 101$ lattice nodes (D3Q19), in x -, y - and z -directions, respectively. We choose to use an inlet velocity in the LB solver as $U_0 = 0.04 \Delta x / \Delta t$, which is sufficiently small to verify the weakly-compressible condition. Hence, given that $L = 50 \Delta x$, the relaxation time in the LB solver is equal to $\bar{\tau} / \Delta t = 0.5 + (U_0 L / Re) / c_s^2 = 0.53$. The solid structure is discretized with a mesh of size $50 \times 50 \times 2$ elements. The common time-step is set as $\Delta t = 0.0008 L / U_0$, which satisfies the numerical stability condition for the explicit Newmark time integrator used in the FE solver.

Figure 15-(a) shows the time evolution of the position in y -direction of the middle point at the trailing edge of the flag, which is compared with the result of Huang and Sung [21] and the one of Lee and Choi [29]. A good agreement can be found with the references in this comparison. Moreover, the drag coefficient $C_d = \mathcal{F} \cdot \mathbf{e}_x / (0.5 \rho_f U_0^2 L^2)$ is shown in Figure 15-(b), where \mathcal{F} denotes the total force computed using Equation (27) and T is the period of the flapping cycle. Once again, by comparing with the result (flag 2) of Tian et al. [46] and the one of Dorschner et al. [11], one may observe a good agreement with the references. Additionally, the flapping amplitude A/L and the Strouhal number $St = fL/U_0$ with $f = 1/T$ are also compared with the results in several recent works in Table 6.

Finally, the proposed IB-RLB coupling method is applied to simulate the 3D flapping flag test-case at a higher Reynolds number $Re = 500$ with $\bar{\tau} / \Delta t = 0.512$, while keeping all the other parameters the same as in the previous case at $Re = 200$. Figure 16 shows the vortical structures in the fluid domain at the two

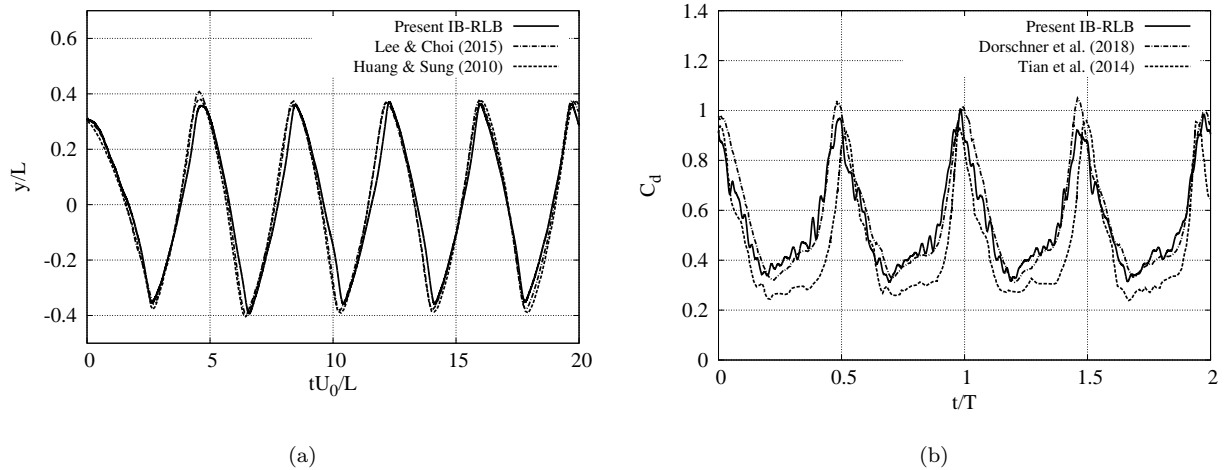


Figure 15: Numerical results of the 3D flapping flag test-case at $Re = 200$: (a) the position in y -direction of the middle point at the trailing edge of the flag; (b) the drag coefficient C_d .

Table 6: Numerical results of the 3D flapping flag test-case at $Re = 200$.

	A/L	St
Present IB-RLB	0.728	0.269
de Tullio & Pascazio [8] (2016)	0.795	0.265
Lee & Choi [29] (2015)	0.752	0.265
Tian et al. (flag 2) [46] (2014)	0.806	0.266
Huang & Sung [21] (2010)	0.780	0.260

Reynolds numbers, which are visualized by using the iso-surface of the Q-criterion. The time histories of the displacement in y -direction of the middle point at the trailing edge, obtained using four mesh resolutions, are shown in Figure 17. Notice that the mesh spacings for the FE and LB solvers remain the same in this mesh convergence study. In addition, the amplitude A and the St number of the flapping motion are summarized in Table 7. One may observe that the numerical results are not very sensitive to the mesh size, especially for the St number. However, we find that the St number in the present result is higher than the one in [21]. This discrepancy may be possibly due to the different modelings of the structural material properties.

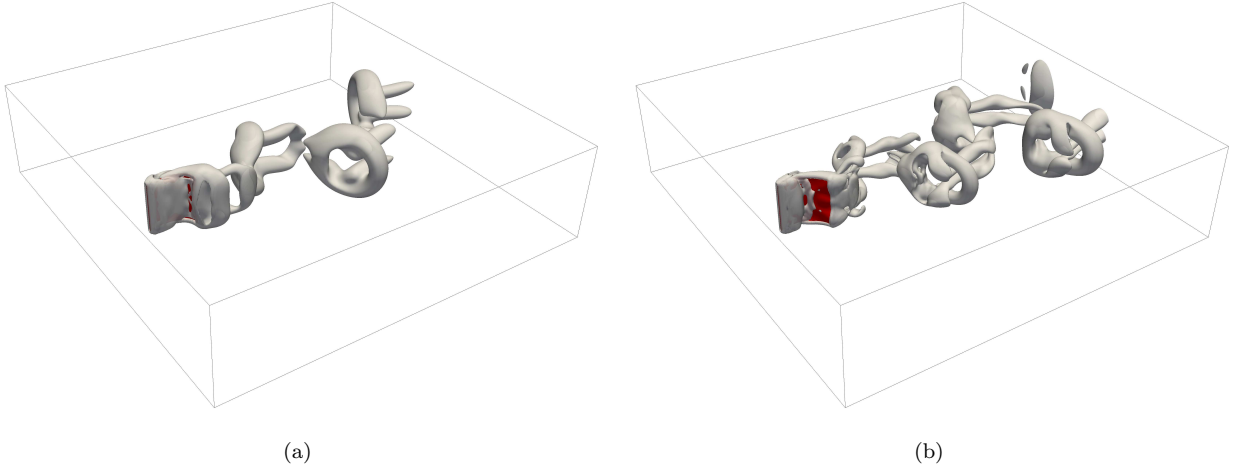


Figure 16: Snapshots at $tU_0/L = 20$ of the vortical structures visualized by means of the iso-surface of the Q-criterion in the 3D flapping flag test-case at two Reynolds numbers: (a) $Re = 200$; (b) $Re = 500$.

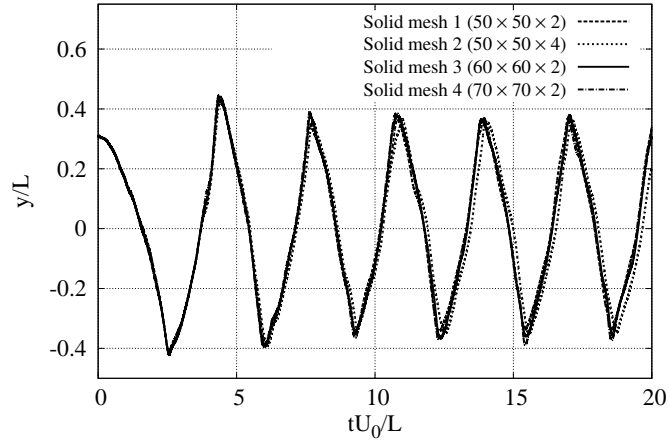


Figure 17: Time histories of the displacement in y -direction of the middle point at the trailing edge with four mesh resolutions in the 3D flapping flag test-case at $Re = 500$.

Table 7: Numerical results of the 3D flapping flag test-case at $Re = 500$ with four mesh resolutions.

Mesh of the flag	A/L	St
$50 \times 50 \times 2$	0.710	0.322
$50 \times 50 \times 4$	0.711	0.323
$60 \times 60 \times 2$	0.727	0.325
$70 \times 70 \times 2$	0.731	0.325

6. Conclusion

In the present paper, the force model effect on the Hermite regularization procedure in LBM is analyzed. It is demonstrated that, with the 2nd-order semi-implicit force model [15], it is necessary to start from the 1st-order term when reconstructing the non-equilibrium part of the distribution \hat{f}_a^{neq} . Based on this Hermite regularization including both the 1st-order and 2nd-order terms, an immersed boundary-regularized lattice Boltzmann (IB-RLB) coupling method is proposed for the numerical simulation of transient fluid-structure interaction (FSI) problems. In the proposed coupling algorithm, the fluid and solid solvers are coupled in a non-staggered way preserving the numerical stability as well as the accuracy of the numerical schemes used in each sub-domain. The proposed IB-RLB coupling method is validated in several numerical test-cases, in which it is observed that:

- Adopting the Hermite regularization procedure [54] does not degrade the convergence order (2nd-order) of LBM in the Taylor-Green vortex test-case.
- Due to the use of the regularization before the collision step, the regularized LBM demands approximately 50% more CPU time than the standard SRT-BGK LBM.
- The regularization can remarkably help reduce the spurious noise generated near an immersed moving solid object, such as an impulsively started plate, while preserving the accuracy of the result.
- By means of the proposed IB-RLB non-staggered coupling method, the frequency lock-in phenomenon in the vortex-induced vibrations of an elastically mounted cylinder can be correctly simulated.
- The proposed IB-RLB coupling method is also validated in some FSI test-cases in the presence of a deformable solid structure, such as a 3D flapping flag. In the FSI3 test-case where the solid-to-fluid density ratio is equal to one, the present method can give a stable numerical simulation.

As expected, the regularization based on the Hermite expansion [54] turns out to be a good candidate that can efficiently stabilize the numerical simulation of FSI problems simulated with the IB-RLB coupling framework, while preserving the accuracy of the numerical methods. As a result, the proposed IB-RLB coupling method

allows one to carry out numerical simulations of FSI problems at [higher](#) Re numbers (still laminar flows) using less discretization points, or in other words, with a small lattice viscosity corresponding to a relaxation parameter $\bar{\tau}$ close to 0.5. This makes the proposed IB-RLB coupling method as accurate as, but much more robust and effective than, the previous IB-SLB one [\[31, 32\]](#).

References

- [1] S. Ansumali and I.V. Karlin. Single relaxation time model for entropic lattice Boltzmann methods. *Physical Review E*, 65:056312, 2002.
- [2] R. Bhardwaj and R. Mittal. Benchmarking a Coupled Immersed-Boundary-Finite-Element Solver for Large-Scale Flow-Induced Deformation. *AIAA Journal*, 50:1638 – 1642, 2012.
- [3] P.L. Bhatnagar, E.P. Gross, and M. Krook. A model for collision processes in gases. I: small amplitude processes in charged and neutral one-component system. *Physical Review*, 94:511, 1954.
- [4] S. Chapman and T.G. Cowling. *The Mathematical Theory of Non-uniform Gases: An Account of the Kinetic Theory of Viscosity, Thermal Conduction and Diffusion in Gases*. Cambridge Mathematical Library. Cambridge University Press, 1970.
- [5] H. Chen, R. Zhang, I. Staroselsky, and M. Jhon. Recovery of full rotational invariance in lattice Boltzmann formulations for high Knudsen number flows. *Physica A: Statistical Mechanics and its Applications*, 362:125 – 131, 2006.
- [6] C. Coreixas, G. Wissocq, G. Puigt, J.F. Boussuge, and P. Sagaut. Recursive regularization step for high-order lattice Boltzmann methods. *Physical Review E*, 96:033306, 2017.
- [7] E. de Langre. Frequency lock-in is caused by coupled-mode flutter. *Journal of Fluids and Structures*, 22:783 – 791, 2006.
- [8] M.D. de Tullio and G. Pascazio. A moving-least-squares immersed boundary method for simulating the fluid-structure interaction of elastic bodies with arbitrary thickness. *Journal of Computational Physics*, 325:201 – 225, 2016.
- [9] P.J. Dellar. An interpretation and derivation of the lattice Boltzmann method using Strang splitting. *Computers and Mathematics with Applications*, 65:129 – 141, 2013.
- [10] W. Dettmer and D. Perić. A computational framework for fluid-rigid body interaction: Finite element formulation and applications. *Computer Methods in Applied Mechanics and Engineering*, 195:1633 – 1666, 2006.

- [11] B. Dorschner, S.S. Chikatamarla, and I.V. Karlin. Fluid-structure interaction with the entropic lattice Boltzmann method. *Physical Review E*, 97:023305, 2018.
- [12] J. Favier, A. Revell, and A. Pinelli. A Lattice Boltzmann - Immersed Boundary method to simulate the fluid interaction with moving and slender flexible objects. *Journal of Computational Physics*, 261:145 – 161, 2014.
- [13] A. Goza and T. Colonius. A strongly-coupled immersed-boundary formulation for thin elastic structures. *Journal of Computational Physics*, 336:401 – 411, 2017.
- [14] H. Grad. On the kinetic theory of rarefied gases. *Communications on Pure and Applied Mathematics*, 2:331 – 407, 1949.
- [15] Z. Guo, C. Zheng, and B. Shi. Discrete lattice effects on the forcing term in the lattice Boltzmann method. *Physical Review E*, 65:046308, 2002.
- [16] Z. Guo, C. Zheng, B. Shi, and Zhao T.S. Thermal lattice Boltzmann equation for low Mach number flows: Decoupling model. *Physical Review E*, 75:036704, 2007.
- [17] T. He, D. Zhou, and Y. Bao. Combined interface boundary condition method for fluid-rigid body interaction. *Computer Methods in Applied Mechanics and Engineering*, 223 - 224:81 – 102, 2012.
- [18] X. He, S. Chen, and D. Doolen. A novel thermal model for the lattice Boltzmann method in incompressible limit. *Journal of Computational Physics*, 146:282 – 300, 1998.
- [19] M. Heil. An efficient solver for the fully coupled solution of large-displacement fluid-structure interaction problems. *Computer Methods in Applied Mechanics and Engineering*, 193:1 – 23, 2004.
- [20] F. Higuera, S. Succi, and R. Benzi. Lattice gas dynamics with enhanced collisions. *Europhysics Letters*, 9(4):345 – 349, 1989.
- [21] W.-X. Huang and H.J. Sung. Three-dimensional simulation of a flapping flag in a uniform flow. *Journal of Fluid Mechanics*, 653:301 – 336, 2010.
- [22] I.V. Karlin, F. Bösch, and S.S. Chikatamarla. Gibbs’ principle for the lattice-kinetic theory of fluid dynamics. *Physical Review E*, 90:031302(R), 2014.
- [23] S. Kollmannsberger, S. Geller, A. Düster, J. Tölke, C. Sorger, M. Krafczyk, and E. Rank. Fixed-grid fluid-structure interaction in two dimensions based on a partitioned lattice Boltzmann and p-FEM approach. *International Journal for Numerical Methods in Engineering*, 79(7):817 – 845, 2009.

- [24] T. Krüger, F. Varnik, and D. Raabe. Efficient and accurate simulations of deformable particles immersed in a fluid using a combined immersed boundary lattice Boltzmann finite element method. *Computers & Mathematics with Applications*, 61:3485 – 3505, 2011.
- [25] A.J.C. Ladd and R. Verberg. Lattice-Boltzmann Simulations of Particle-Fluid Suspensions. *Journal of Statistical Physics*, 104:1191 – 1251, 2001.
- [26] P. Lallemand and L.S. Luo. Theory of the lattice Boltzmann method: Dispersion, dissipation, isotropy, Galilean invariance, and stability. *Physical Review E*, 61:6546, 2000.
- [27] J. Latt and B. Chopard. Lattice Boltzmann method with regularized pre-collision distribution functions. *Mathematics and Computers in Simulation*, 72:165 – 168, 2006.
- [28] J. Latt, B. Chopard, O. Malaspinas, M. Deville, and A. Michler. Straight velocity boundaries in the lattice Boltzmann method. *Physical Review E*, 77:056703, 2008.
- [29] I. Lee and H. Choi. A discrete-forcing immersed boundary method for the fluid-structure interaction of an elastic slender body. *Journal of Computational Physics*, 280:529 – 546, 2015.
- [30] Q. Li, K.H. Luo, Y.L. He, Y.J. Gao, and W.Q. Tao. Coupling lattice Boltzmann model for simulation of thermal flows on standard lattices. *Physical Review E*, 85:016710, 2012.
- [31] Z. Li and J. Favier. A non-staggered coupling of finite element and lattice Boltzmann methods via an immersed boundary scheme for fluid-structure interaction. *Computers & Fluids*, 143:90 – 102, 2017.
- [32] Z. Li, J. Favier, U. D’Ortona, and S. Poncet. An immersed boundary-lattice boltzmann method for single- and multi-component fluid flows. *Journal of Computational Physics*, 304:424 – 440, 2016.
- [33] N.S. Martys, X. Shan, and H. Chen. Evaluation of the external force term in the discrete Boltzmann equation. *Physical Review E*, 58:6855 – 6857, 1998.
- [34] K.K. Mattila, L.A. Hegele Jr, and P.C. Philippi. Investigation of an entropic stabilizer for the lattice-boltzmann method. *Physical Review E*, 91:063010, 2015.
- [35] K.K. Mattila, P.C. Philippi, and L.A. Hegele Jr. High-order regularization in lattice-Boltzmann equations. *Physics of Fluids*, 29:046103, 2017.
- [36] A. Montessori, G. Falcucci, P. Prestininzi, M. La Rocca, and S. Succi. Regularized lattice Bhatnagar-Gross-Krook model for two- and three-dimensional cavity flow simulations. *Physical Review E*, 89:053317, 2014.

- [37] N.M. Newmark. A method of computation for structural dynamics. *Journal of the Engineering Mechanics Division*, 85, 1959.
- [38] A. Pinelli, I.Z. Naqavi, U. Piomelli, and J. Favier. Immersed-boundary methods for general finite-difference and finite-volume Navier-Stokes solvers. *Journal of Computational Physics*, 229:9073 – 9091, 2010.
- [39] T.K. Prasanth and S. Mittal. Vortex-induced vibrations of a circular cylinder at low reynolds numbers. *Journal of Fluid Mechanics*, 594:463 – 491, 2008.
- [40] Y.H. Qian, D. D’Humières, and P. Lallemand. Lattice BGK models for Navier-Stokes equation. *Europhysics Letters*, 17(6):479 – 484, 1992.
- [41] D. Ricot, S. Marié, P. Sagaut, and C. Bailly. Lattice Boltzmann method with selective viscosity filter. *Journal of Computational Physics*, 228:4478 – 4490, 2009.
- [42] A.M. Roma, C.S. Peskin, and M.J. Berger. An adaptive version of the immersed boundary method. *Journal of Computational Physics*, 153:509 – 534, 1999.
- [43] X. Shan, X.F. Yuan, and H. Chen. Kinetic theory representation of hydrodynamics: a way beyond the Navier-Stokes equation. *Journal of Fluid Mechanics*, 550:413 – 441, 2006.
- [44] S.P. Singh and S. Mittal. Vortex-induced oscillations at low reynolds numbers: Hysteresis and vortex-shedding modes. *Journal of Fluids and Structures*, 20:1085 – 1104, 2005.
- [45] S. Succi. Lattice Boltzmann beyond Navier-Stokes: Where do we stand? *AIP Conference Proceedings*, 1786:030001, 2016.
- [46] F.B. Tian, H. Dai, H. Luo, J.F. Doyle, and B. Rousseau. Fluid-structure interaction involving large deformations: 3D simulations and applications to biological systems. *Journal of Computational Physics*, 258:451 – 469, 2014.
- [47] S. Turek and J. Hron. *Proposal for Numerical Benchmarking of Fluid-Structure Interaction between an Elastic Object and Laminar Incompressible Flow*, volume 53 of *Lecture Notes in Computational Science and Engineering*. Springer Berlin Heidelberg, 2006.
- [48] M. Vanella and E. Balaras. A moving-least-squares reconstruction for embedded-boundary formulations. *Journal of Computational Physics*, 228:6617 – 6628, 2009.
- [49] Y. Wang, C. Shu, C.J. Teo, and J. Wu. An immersed boundary-lattice Boltzmann flux solver and its applications to fluid-structure interaction problems. *Journal of Fluids and Structures*, 54:440 – 465, 2015.

- [50] C.H.K. Williamson and R. Govardhan. Vortex-induced vibrations. *Annual Review of Fluid Mechanics*, 36:413 – 455, 2004.
- [51] L. Xu, F.B. Tian, J. Young, and J.C.S. Lai. A novel geometry-adaptive Cartesian grid based immersed boundary-lattice Boltzmann method for fluidstructure interactions at moderate and high Reynolds numbers. *Journal of Computational Physics*, 375:22 – 56, 2018.
- [52] X. Yang, X. Zhang, Z. Li, and G. He. A smoothing technique for discrete delta functions with application to immersed boundary method in moving boundary simulations. *Journal of Computational Physics*, 228:7821 – 7836, 2009.
- [53] H. Zhang, H. Fey, and B.R. Noack. On the transition of the cylinder wake. *Physics of Fluids*, 7:779 – 794, 1995.
- [54] R. Zhang, X. Shan, and H. Chen. Efficient kinetic method for fluid simulation beyond the Navier-Stokes equation. *Physical Review E*, 74:046703, 2006.

Appendix

In 2006, Latt and Chopard [27] proposed a regularization procedure based on the computation of the gradient of the macroscopic velocity. Here, we show that this regularization formula [27] can also be derived by means of the Hermite expansion. Body force is not considered in this demonstration for the sake of simplicity.

In the Chapman-Enskog analysis [4] on the LBE, the distribution function and the derivative operators are developed as

$$\begin{cases} \bar{f}_a = \varepsilon^0 \bar{f}_a^{(0)} + \varepsilon^1 \bar{f}_a^{(1)} + \varepsilon^2 \bar{f}_a^{(2)} + \mathcal{O}(\varepsilon^3), \\ \frac{\partial}{\partial t} = \varepsilon \frac{\partial}{\partial t_1} + \varepsilon^2 \frac{\partial}{\partial t_2}, \\ \nabla = \varepsilon \nabla_1, \end{cases} \quad (\text{A.1})$$

where ε is the expansion parameter, $t_1 = \varepsilon t$, $t_2 = \varepsilon^2 t$ and $\mathbf{x}_1 = \varepsilon \mathbf{x}$. Thus, at each scale of ε , one has

$$\begin{cases} \mathcal{O}(\varepsilon^0) : & \bar{f}_a^{(0)} = f_a^{eq}, \\ \mathcal{O}(\varepsilon^1) : & \frac{\partial \bar{f}_a^{(0)}}{\partial t_1} + \boldsymbol{\xi}_a \cdot \nabla_1 \bar{f}_a^{(0)} = -\frac{1}{\bar{\tau}} \bar{f}_a^{(1)}, \\ \mathcal{O}(\varepsilon^2) : & \frac{\partial \bar{f}_a^{(0)}}{\partial t_2} + \left(1 - \frac{\Delta t}{2\bar{\tau}}\right) \left(\frac{\partial \bar{f}_a^{(1)}}{\partial t_1} + \boldsymbol{\xi}_a \cdot \nabla_1 \bar{f}_a^{(1)}\right) = -\frac{1}{\bar{\tau}} \bar{f}_a^{(2)}. \end{cases} \quad (\text{A.2})$$

Based on Equation (A.2) and the equilibrium distribution function f_a^{eq} given in Equation (2), the 2nd-order moment $\mathbf{\Pi}^{(1)}$ of $\bar{f}_a^{(1)}$ can be obtained as [30]

$$\begin{aligned}\mathbf{\Pi}^{(1)} &= \sum_a \boldsymbol{\xi}_a \otimes \boldsymbol{\xi}_a \bar{f}_a^{(1)}, \\ &= -\bar{\tau} \rho c_s^2 \left(\nabla_1 \mathbf{v} + (\nabla_1 \mathbf{v})^\top \right) + \bar{\tau} \nabla_1 \cdot (\rho \mathbf{v} \otimes \mathbf{v} \otimes \mathbf{v}),\end{aligned}\tag{A.3}$$

in which the last term on the right hand side can be neglected in low Mach number limit, which is the case in weakly-compressible flow. In addition, assuming $\bar{f}_a^{neq} \simeq \varepsilon \bar{f}_a^{(1)}$ gives the 2nd-order moment $\mathbf{\Pi}^{neq}$ of \bar{f}_a^{neq} as

$$\begin{aligned}\mathbf{\Pi}^{neq} &= \sum_a \boldsymbol{\xi}_a \otimes \boldsymbol{\xi}_a \bar{f}_a^{neq}, \\ &\simeq \sum_a \boldsymbol{\xi}_a \otimes \boldsymbol{\xi}_a \varepsilon \bar{f}_a^{(1)}, \\ &\simeq -\varepsilon \bar{\tau} \rho c_s^2 \left(\nabla_1 \mathbf{v} + (\nabla_1 \mathbf{v})^\top \right), \\ &= -\bar{\tau} \rho c_s^2 \left(\nabla \mathbf{v} + (\nabla \mathbf{v})^\top \right).\end{aligned}\tag{A.4}$$

Since, by definition, one has $\sum_a \bar{f}_a^{neq} = 0$, $\mathbf{\Pi}^{neq}$ can then be related with the 2nd-order expansion coefficient $\mathbf{a}_{neq}^{(2)}$ of the Hermite expansion of \bar{f}_a^{neq} in the following way

$$\mathbf{a}_{neq}^{(2)} = \sum_a \left(\frac{\boldsymbol{\xi}_a \otimes \boldsymbol{\xi}_a}{c_s^2} - \mathbf{I} \right) \bar{f}_a^{neq} = \frac{\mathbf{\Pi}^{neq}}{c_s^2} \simeq -\bar{\tau} \rho \left(\nabla \mathbf{v} + (\nabla \mathbf{v})^\top \right).\tag{A.5}$$

Without the body force term, one has $\mathbf{a}_{neq}^{(0)} = 0$ and $\mathbf{a}_{neq}^{(1)} = \mathbf{0}$. As a consequence, the regularized non-equilibrium part of the distribution function \hat{f}_a^{neq} can be reconstructed by means of the Hermite expansion as

$$\begin{aligned}\hat{f}_a^{neq} &= w_a \sum_{n=0}^2 \frac{1}{n!} \mathbf{a}_{neq}^{(n)} : \mathcal{H}_a^{(n)}, \\ &= w_a \frac{1}{2!} \mathbf{a}_{neq}^{(2)} : \mathcal{H}_a^{(2)}, \\ &\simeq \frac{w_a}{2} \left(-\bar{\tau} \rho \left(\nabla \mathbf{v} + (\nabla \mathbf{v})^\top \right) \right) : \left(\frac{\boldsymbol{\xi}_a \otimes \boldsymbol{\xi}_a}{c_s^2} - \mathbf{I} \right),\end{aligned}\tag{A.6}$$

which is just the regularization formula proposed by Latt and Chopard [27] for weakly-compressible fluid flows ($d\rho/\rho \ll 1$).